We are IntechOpen, the world's leading publisher of Open Access books
Built by scientists, for scientists

6,900
Open access books available

185,000
International authors and editors

200M
Downloads

154
Countries delivered to

Our authors are among the

TOP 1%
most cited scientists

12.2%
Contributors from top 500 universities

BOOK CITATION INDEX
CLARIVATE ANALYTICS
INDEXED

WEB OF SCIENCE™

Selection of our books indexed in the Book Citation Index
in Web of Science™ Core Collection (BKCI)

Interested in publishing with us?
Contact book.department@intechopen.com

A Method for Optical Proximity Correction of Thermal Processes: Orthogonal Functional Method

Sang-Kon Kim
Hanyang University
South Korea

1. Introduction

Pattern reduction has created a great deal of interest in finding effective methods to reduce the feature sizes of microelectronic and data-storage devices. These methods are divided between top-down approach such as photolithography and bottom-up approach such as self-assembly. For below 32 nm node technology, top-down approach has obstacles such as diffraction-limited resolution and high cost of ownership and bottom-up approach has obstacles such as the insufficient support of processes and mass production.

Thermal treatment is a new process extension technique using current-day lithography equipment and chemically amplified resists (CARs). In the lithography process, thermal processes are softbake (SB), post-exposure bake (PEB), and thermal reflow. The purpose of SB is to remove excess solvent after spin coating, relieve strain in the solid film, and provide better adhesion to the substrate. The purpose of PEB is to reduce the standing wave effect and, thus, increase linewidth control and resolution. The purpose of thermal reflow is to reduce the pattern size by using thermal heating at temperatures about the glass transition temperature of the resist after development. These three kinds of thermal processes are essentially the same for heat treatment, but they have different effects on CD. Hence, it is required to understand mechanism behaviors that drive photo resist image and to deal with optical proximity effects (OPEs) due to thermal processes. OPE is quite severe as the critical dimensions (CDs) shrink down to the sub-30 nm patterns. Although the simulation parameters are not used to analyze the chemical phenomena of thermal processes, the CD bias after thermal reflow can be predicted in the linear system. Through the optical proximity correction (OPC), the distorted image from OPE can be manipulated back to the original design. However, the thermal affects of CD is the non-linear system, so that the prediction of OPE is not easy. Hence, the understanding of mechanistic behaviors that drive photo resist image can make the physically corrected resist model, and achieve the best prediction of resist images across multiple process conditions.

One of the most critical issues for sub-50-nm patterning is patterning a fine contact hole (C/ H). The resolution performance of contact hole patterns is lower than that of line and space patterns because the depth of focus (DOF) for patterning contact holes is insufficient due to the low aerial-image contrast. The resist reflow process is a good method due to its simplicity without the additional complex process steps and due to its efficient technique

with the appropriate selection of the resist properties and the thermal loading process conditions. However, it is difficult to predict the results of the thermal flow and the process optimization. Thus, the layout designs are only done by trial and error because there are so many effective parameters, such as baking temperature, baking time, resist original characteristics, resist volume surrounding C/ H, initial C/ H size and shape, and C/ H array. To predict the resist shrinkage of resist reflow, according to the experimental data fitting method, the shrink bias can only be expressed as the functional relationship of the baking temperature, normalized resist volume, and native property of resist. By the quantitative analysis of the shrink bias for the baking temperature, the relationship can be expressed as a linear equation. The simple equation helps in understanding the characteristics of the resist reflow and also shows mechanism for process stabilization.

The objectives of the work presented in this chapter are to make the physically corrected resist model based on the understanding of mechanistic behaviors that drive photo resist image, to achieve the best prediction of resist images across multiple process conditions, and to develop a general simulation approach of OPC to reduce the OPEs during lithography thermal processes. Section 2 describes the modeling of the lithography process, the modeling of thermal processes, and the simulation of those thermal processes. Section 3 describes thermal bias based on the simulation of the models in section 2 and introduces the orthogonal functional method. The simulation results of SB and PEB are used by the comparison of a commercial tool, SOLID-C (Shynopsys Inc.)[1]. Section 4 describes the analysis for the below 45 nm contact hole (C/ H) pattern for a KrF 248 nm CAR and 32 nm C/ H pattern for a ArF 193 nm CAR. Two stage corrections of model-based OPC are performed by using the orthogonal functional method. Section 5 describes the conclusion of this chapter.

2. Thermal process model

2.1 Simulation benchmarking for the whole resist process

For the semiconductor industry, lithography is the key technology driver and a significant economic factor, currently representing over thirty five percent of the chip manufacturing cost. Significant investments from research and development to device commercialization will improve the infrastructure of this vital technology and maintain industry growth. The cost of experiments is now very large and the complexity of lithographic patterns and processes (e.g. phase shift and chemical amplification) is too big to ignore the simulation. To support this, the availability, accuracy, and easy use of lithography simulation must be improved [2]. As a research tool, lithography simulation performs experiments that would be difficult or impossible to do by any other way.

As a process development and process transfer tool, a simulation tool can quickly evaluate options, optimize processes, or save time and money by reducing the number of experiments in the fab. As a manufacturing tool, it can troubleshoot process problems, determine optimum process settings, and aid in decision making by providing facts to support engineering judgment and intuition. As a learning tool, its proper application allows the user to learn efficiently the lithography process. Hence, performing the physical and molecular simulation can be helpful to analyze, understand, and predict the lithography technologies for gigabit era.

Figure 1 shows the structure of lithography simulation. These simulation models are used for spin coating, soft bake, illumination, exposure, delay, post exposure bake, development,
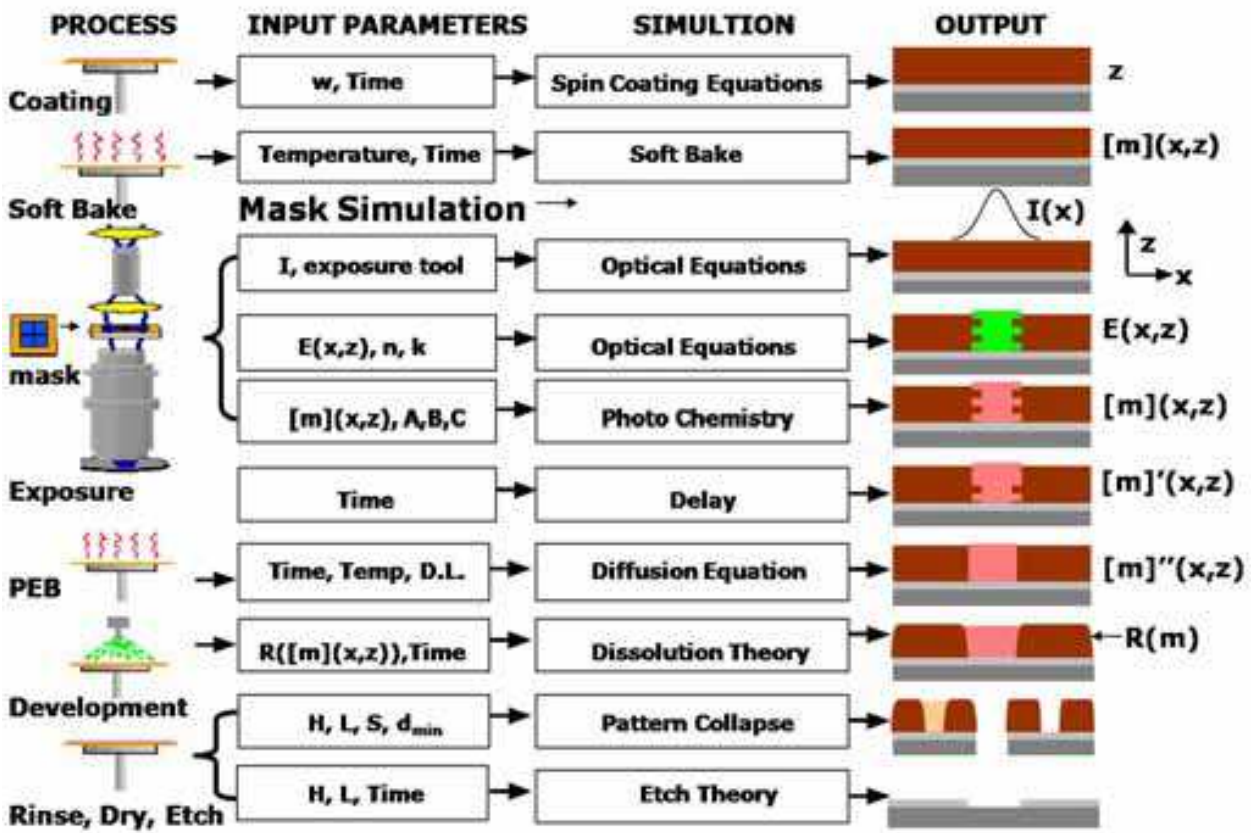
W: spin velocity, I: intensity, E(x,z):exposure, n:refractive index, k:absorbtion index, [m](x,z): photo acid generator (PAG), A, B, C; Dill's parameters, [m]'(x,z): PAG after delay, [m]''(x,z): PAG after PEB, R([m])(x,z): dissolution rate, H: pattern height, L: pattern width, S: line width, d_{min}: minimum line width.

Fig. 1. Simulation modeling

rinse, dry, and etch processes. For the spin coating model, input parameters are spin velocity and time. Resist thickness is calculated by solving the Navier-Stokes equation or the convective diffusion equation. Irregular surfaces caused by spin coating and solvent evaporation are not considered. In the soft bake model, input parameters are temperature and time. The photo acid compound (PAC) is calculated.

The illumination part is modeled as the projection lens system. Aerial image is calculated by solving the optical equations due to illumination parameters as input parameters. In the bulk model, bulk image inside resist is calculated by using the multiple thin layer interference theory and the Berning theory instead of the rigorous solution for the Maxwell's equations. During the exposure simulation, the PAC for the non-CAR (chemically amplified resist) and the photo acid generator (PAG) for the CAR are calculated by Dill's model. In the delay model, the input parameter such as delay time affects the PAC or the PAG. For the post exposure bake (PEB) model, the modified PAC or PAG is calculated by solving diffusion equation due to input parameters such as time, temperature, and diffusion length. In the development model, the dissolution rate is calculated by using the dissolution theory. Resist profile is shown by using the ray tracing algorithm. Etch simulation shows the impact

of the final resist profile shape on the quality of the etched pattern in the substrate by using the Hamilton-Jacobi equation of the higher dimensional function. LAVA (the Lithography Analysis using Virtual Access) [3], PROLITH (the Positive Resist Optical LITHography model) [4], and SOLID-C (the Simulation of Optical Lithography in three Dimensions for the personal Computer) [1] are the lithography simulators for the personal computer among the academic and commercial tools.

2.2 Softbake (SB)

SB is a thermal process before exposure. During SB, the occurrence of photo-chemical reactions depends largely on the diffusion ability of a photoactive compound in a photoresist, and the free volume content of a photoresisst significantly affects its lithographic properties. In terms of the process physics, since the solvent of the resist is evaporated, the thickness of the resist shrinks, and the refractive index and the density of the resist are changed. This process can be a combination of solvent evaporation, solvent diffusion, and polymer compaction. The solvent concentration $S(z)$ in the solvent evaporation-diffusion process is

$$\frac{dS(z)}{dt} = -k_{evap} \bullet S(z) \bullet \delta(z) + \nabla D_S \nabla S(z), \tag{1}$$

where k_{evap} is the evaporation rate constant and D_S is the solvent diffusion coefficient. The free volume of the polymer film is

$$v_f = (1 - \chi_S) \bullet v_g + \alpha \bullet (T - T_g) + \chi_S \bullet \beta, \tag{2}$$

where χ_S is the mass fraction of solvent, T_g is the glass transition temperature of the pure polymer, v_g is the free volume of the pure polymer at T_g, α is the differential thermal expansion coefficient above the T_g, and ρ is density-scaled fractional volume parameter. The solvent diffusivity is

$$D = D_o \exp\left(-B\left(\frac{1}{v_f} - \frac{1}{v_g}\right)\right), \qquad v_f > v_g, \qquad D = D_o, \quad v_f < v_g, \tag{3}$$

where D_o is the diffusion coefficient at T_g and B is the free volume efficiency parameter. The refractive index of the resist is

$$\eta_{resist} = \left(1 - \sum_i \chi_i\right) \bullet \eta_{polymer} + \sum_i \chi_i \bullet \eta_i, \tag{4}$$

where $\eta_{polymer}$ is the refractive index of the resist polymer, χ_i is the fraction of the i-th resist component remaining after the softbake step, and η_i is the complex refractive index of the i-th component [5].

2.3 Post-exposure Bake (PEB)

A typical positive-type CAR is composed of a polymer resin, a photoacid generator (PAG), and a dissolution inhibitor. When the CAR is exposed to light, acid is generated by

conversion of the PAG. The acid concentration is related to the exposure dose through Dill's ABC parameters. During PEB, this initial acid derives the de-protection reaction with a thermal acid-catalyzed reaction that alters the development rate of the resist. Exposing the resist to deep ultraviolet (DUV) light generates acid from the PAG. During a subsequent PEB, the photogenerated acid catalyzes a thermally induced reaction that cleaves the dissolution inhibitor groups (protecting groups), rendering the reacted (deprotected) region soluble in the aqueous developer. Meanwhile, the acid diffuses from a high-dose region to a low-dose region, washing out standing waves and causing the reacted region to be larger than the initially exposed region. In addition, most CARs exhibit volume shrinkage after the PEB step due to desorption of volatile group byproducts that are created during the bake. The PAG concentration changes during exposure and has been described by

$$\frac{d[PAG]}{dt'} = -C[PAG]I \rightarrow [PAG] = [PAG]_o e^{-CIt'}, \tag{5}$$

$$[A]_{dose} = [PAG]_o - [PAG] = [PAG]_o \left(1 - e^{-CE}\right), \tag{6}$$

where A is the acid and exposure dose (E) is the multiplication of intensity (I) to exposure time (t'). The acid concentration changes during PEB and has been described by

$$\frac{d[A]}{dt} = -k_{loss} \bullet [A] - k_{quench} \bullet [A] \bullet [B] + \nabla \bullet \left(D_{acid}\nabla[A]\right), \tag{7}$$

$$\frac{d[B]}{dt} = -k_{quench} \bullet [A] \bullet [B], \tag{8}$$

$$\frac{d[M]}{dt} = -k_{amp} \bullet [M] \bullet [A]^n, \tag{9}$$

where M is the protecting group of the polymer resin, B is the base quencher, k_{amp} is the acid-catalyzed deprotection rate, k_{loss} is the acid loss reaction rate, k_{quench} is the acid neutralization rate, and t is the PEB time.
The acid diffusivity is

$$D_{acid} = D_0 \exp\left(\frac{\alpha M}{1 + \beta M}\right), \quad D_0 = A_r \exp\left(-\frac{E_a}{RT}\right), \tag{10}$$

where α and β are constants, E_a is the thermolytic decomposition activation energy, A_r is the Arrhenius coefficient, and R is the Boltzmann constant.
Table I shows the simulated parameters of the 90-nm line and space pattern. 140-nm mask pattern is used for the profile of a 90-nm L/S pattern after the development process.
Figure 2 shows simulation results for CDs for overbake of SB and PEB for isolated 94-nm line and 90-nm L/S patterns. When the SB time is increased in Fig. 2 (a), the CD becomes larger, and then saturate. When the PEB time is increased in Fig. 2 (b), the CD decreases to below 40 nm. In the L/S patterns, the underbake of SB and the overbake of PEB can be used for 45-nm pattern formation. In the active area of Fig. 2, the CD sensitivity of the PEB time (2.86 nm/s) is larger than that of the SB time (0.26 nm/s).

- **Mask Pattern**
  90 nm isolated Line and Space (L/ S) pattern
- **Modeling Options**
  Image Calculation Model: Scalar
- **Stepper Parameters**
  Illumination: Convential-partially coherent
  Defocus: 0.0 μm,   Wavelength: 193 nm
  Illumination Pupil Shape: Dipole(radius: 0.5, holesize: 0.3, angle: 45)
  Numerical Aperture (NA): 0.8, Aberrations: none
  Flare[%]: 0
- **Film Stack**
  Layer 1: 390-nm resist, refraction : 1.72 - j0.0
  Layer 2: 82-nm AR^{TM}19, refraction : 1.79 - j0.4
  Layer 3: Silicon, refraction : 6.522 - j2.705
- **Prebake Parameters**
  Temperature: 120°C
  Time: 60 s
- **Exposure Parameters**
  Exposure Dose: 15 mJ/ cm^2
  A: 0.01 (1/ μm), B: 0.5 (1/ μm) , C: 0.03 cm^2/ mJ
- **Post-Exposure Bake Parameters**
  Diffusion Length: 0.035 μm
  Temperature: 130 °C
  Time: 77 s,   Q: 0.067
  k_{amp} (1/ s): 0.75, k_{loss} (1/ s): 2.3x10^{-5}
  Resist Type: Positive
  Exponent n: 2
  Resist thickness reduction parameter: alpha: 1.77, beta: 0.02
  Activation Energy E_2: 0 eV
- **Develop Parameters**
  Development Model: Enhanced notch model
  Time: 45 s,
  R_{min}: 2x10^{-5} nm/ s R_{max}: 0.045 μm/ s
  R_{Res}: 0.0187   n: 1.61   l: 9.84

Table I. Parameters of the 90 nm line and space pattern.

Although the CD sensitivity of thermal parameters can be different due to other process parameters, the CD sensitivity of the PEB temperature is larger than that of the PEB time in the simulation of the L/ S patterns. Both CD sensitivities are larger when the target pattern size is smaller.

Figure 3 shows boundary movements of the acid and the inhibitor concentration due to the extended times of SB and PEB for an isolated 94-nm line pattern. Those resist bulk images are the distributions of acid concentration after exposure and inhibitor concentration after PEB at a SB time of 120 s in Figs. 3 (a) and (c) and at a SB time of 10 s in Figs. 3 (b) and (d).
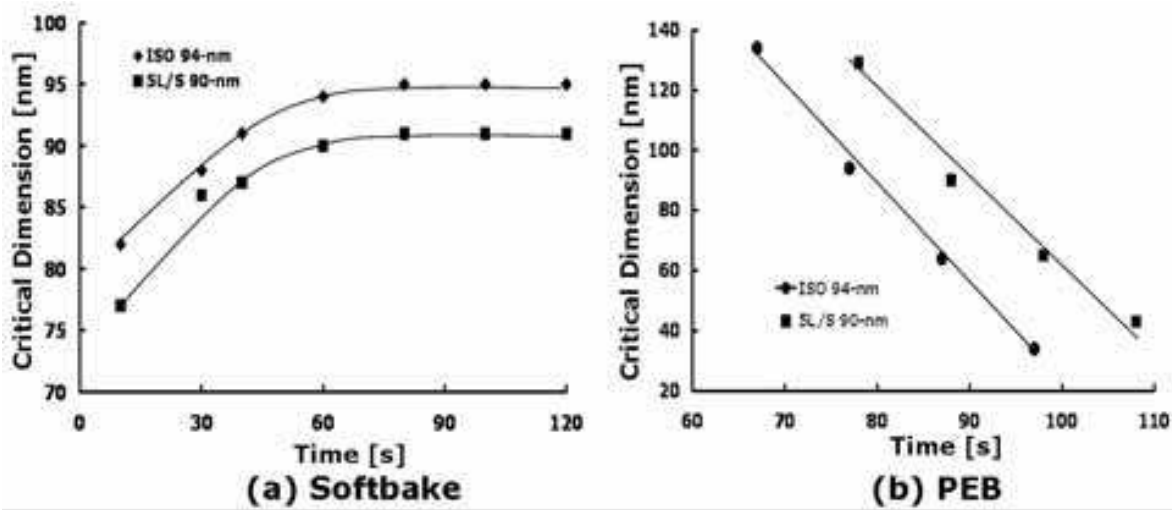
Fig. 2. Simulation results for the critical dimensions (a) SB and (b) PEB for isolated 94-nm line and 90-nm line and space (L/ S) patterns.
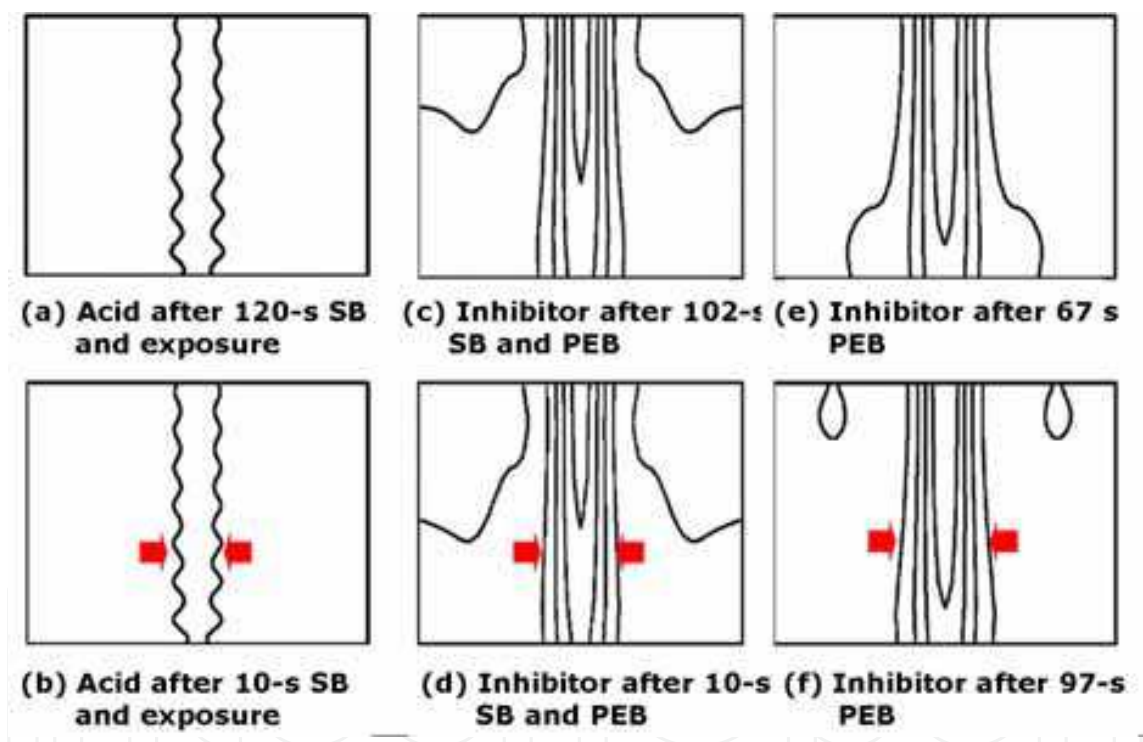

Fig. 3. Resist bulk images of (a) acid concentration after exposure and (c) inhibitor concentration after PEB at a SB time of 120 s, (b) the acid concentration after exposure and (d) inhibitor concentration after PEB at a SB time of 10 s, and inhibitor concentrations at PEB times of (e) 67 s and (f) 97 s.

Figures 3 (e) and (f) show inhibitor concentrations at PEB time of 67 s and 97 s, respectively. Figures (b), (d), and (f) for small patterns can be distinguished from Figs. (a), (c), and (e) for large patterns. Hence, for small pattern formation, the boundaries of acid and inhibitor concentrations move to the center of horizontal axis and become dense. A small SB time and a larger PEB time make the boundaries of the acid and the inhibitor concentrations dense at the center of the horizontal axis.

2.4 Thermal reflow process

Thermal reflow, as a resolution-enhancement technique, is a good method without any additional complex process steps and with appropriate selection of the resist properties and thermal loading process conditions. The thermal reflow process is used to reduce the pattern size of a resist by thermally heating the resist over its glass transition temperature after the development process. When the resist is heated over its glass transition temperature, the bonding of the synthesized resist is reduced and its mobility is improved. The three-dimensional structure of the synthesized resist is changed, and the contact hole (C/ H) pattern size is shrunk due to the additional thermal energy.

However, it is difficult to predict the results of thermal reflow and process optimization, one reason being the optical proximity (or process) effects (OPEs), such as the impact of the image distortion. The OPEs of thermal reflow becomes quite severe as the critical dimensions shrink down to sub-50 nm patterns. If the physics governing a particular OPE is known through experiment and simulation, the distortion can be predicted and modeled. Even when the physics that govern the systematic effects are not fully understood, it still could be modeled if sufficient simulated data are available. Although the simulation parameters are not used to analyze the chemical phenomena of thermal reflow, the critical dimension bias after resist reflow can be predicted in a linear system by using the fitting function of experimental data. Through the optical proximity correction (OPC), the distorted image can be manipulated back to the original designed image.

2.4.1 Boundary-movement method

Boundary movement represents the boundary as a geometric model and solves the partial differential equations for boundary motion. The level-set method is more accurate and efficient than the Lagrangian-type method. The level-set function $\psi(x,y,t)$ is defined as the distance of a point (x,y) to the boundary of the geometry under consideration. The point (x,y) in the geometry boundary is

$$\psi(x,y,t) = 0. \tag{11}$$

Assuming that each boundary point moves along its surface normal,

$$\frac{\partial \psi(x,y,t)}{\partial t} + V|\nabla \psi(x,y,t)| = 0, \tag{12}$$

where V is velocity (μm/ s) of movement. The basic equation system of fluid flow consists essentially of the continuity equation and the conservation equations of momentum and energy. Under the condition that fluid is incompressible and Newtonian, the continuity equation in two dimensions is

$$\frac{\partial v}{\partial x} + \frac{\partial u}{\partial y} = 0, \tag{13}$$

where v and u are the velocity components in the x and y directions, respectively. The conservation equations of momentum are

$$\rho\left(\frac{\partial v}{\partial t} + v\frac{\partial v}{\partial x} + u\frac{\partial v}{\partial y}\right) + \frac{\partial p}{\partial x} = \mu\left(\frac{\partial^2 v}{\partial x^2} + \frac{\partial^2 v}{\partial y^2}\right) + \rho g_x, \tag{14}$$

$$\rho\left(\frac{\partial u}{\partial t}+v\frac{\partial u}{\partial x}+u\frac{\partial u}{\partial y}\right)+\frac{\partial p}{\partial y}=\mu\left(\frac{\partial^2 u}{\partial x^2}+\frac{\partial^2 u}{\partial y^2}\right)+\rho g_y, \tag{15}$$

where p is pressure and ρ is density. The components of gravitational acceleration in the x and y directions are denoted by g_x and g_y, respectively. The symbol μ is fluid viscosity [kg/ m•s]. When the velocity component in the y-direction is negligibly small compared to that in the x-direction, from Eqs. (13) and (14)

$$\frac{\partial v}{\partial x}=0, \tag{16}$$

$$\rho\left(\frac{\partial v}{\partial t}\right)+\frac{\partial p}{\partial x}=\mu\left(\frac{\partial^2 v}{\partial x^2}\right)+\rho g_x. \tag{17}$$

If the gravitational acceleration g_x is negligible, then Eqs. (16) and (17) above can be approximated as

$$\rho\left(\frac{\partial v}{\partial t}\right)=\mu\left(\frac{\partial^2 v}{\partial x^2}\right). \tag{18}$$

If we assume that Eq. (18) is the standard diffusion equation, the thermal reflow length is

$$L=\sqrt{\frac{\mu}{\rho}t}. \tag{19}$$

The boundary point from Eq. (12) moves such that

$$\psi(x,y,t+\Delta t)=\psi(x,y,t)-L\left|\nabla\psi(x,y,t)\right|, \tag{20}$$

where the thermal reflow length (L) is $\Delta t \cdot v$, because the length can be represented as the product of velocity and time.
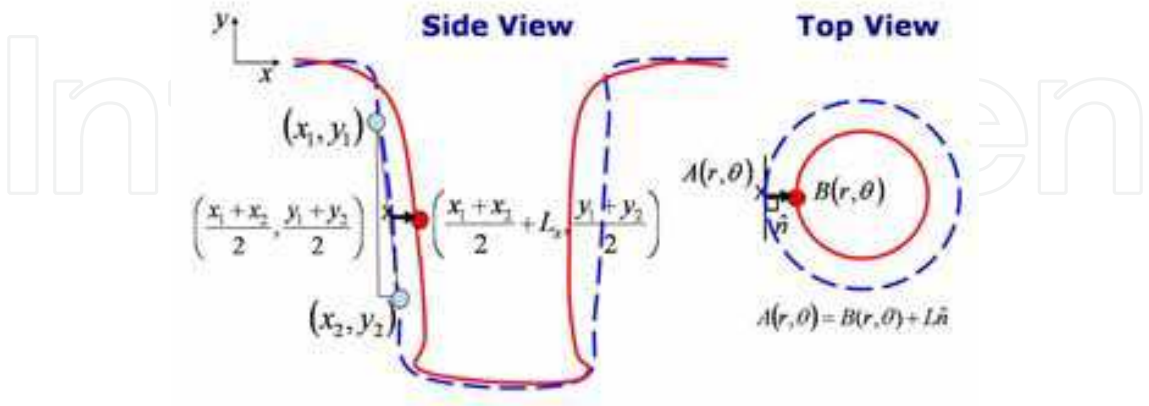

Fig. 4. Thermal flow length.

Figure 4 shows the movement of point (x_1, y_1) and point (x_2, y_2) using the thermal reflow length. After the midpoint of point (y_1, y_1) and point (y_2, y_2) is calculated, this midpoint is moved to thermal reflow length due to time and temperature.

Piecewise-linear	Polynomial
$\mu(T) = \mu_n + (\mu_{n+1} - \mu_n)/(T_{n+1} - T_n) * (T - T_n)$ (a)	$\mu(T) = A_1 + A_2 T + A_3 T^2 + \ldots$ (e)
Piecewise-polynomial	**Sutherland's law**
For $T_{min,1} < T < T_{max,1}$ $\mu(T) = A_1 + A_2 T + A_3 T^2 + \ldots$ (b)	$\mu(T) = C_1 T^{3/2}/(T - C_2)$ (f) or
For $T_{min,2} < T < T_{max,2}$ $\mu(T) = B_1 + B_2 T + B_3 T^2 + \ldots$ (c)	$\mu(T) = \mu_0 (T/T_0)^{3/2} (T_0 + S)/(T + S)$ (g)
Power law	**Standard Arrhenius form (supposed)**
$\mu(T) = BT^n$ (g) or $\mu(T) = \mu_0 (T/T_0)^n$ (d)	$\mu(T) = \mu_0 \exp(E/(RT))$ (h)

Table II. Viscosities as a function of temperature.

Viscosity (μ) is related to the fluid's resistance to motion and is an important aspect of rheology. Viscosity is determined by relating the velocity gradient in fluids to the shear force causing flow to occur. To define the viscosity equation as a function of temperature, viscosity equations in Table II are fitted to the experiment data.
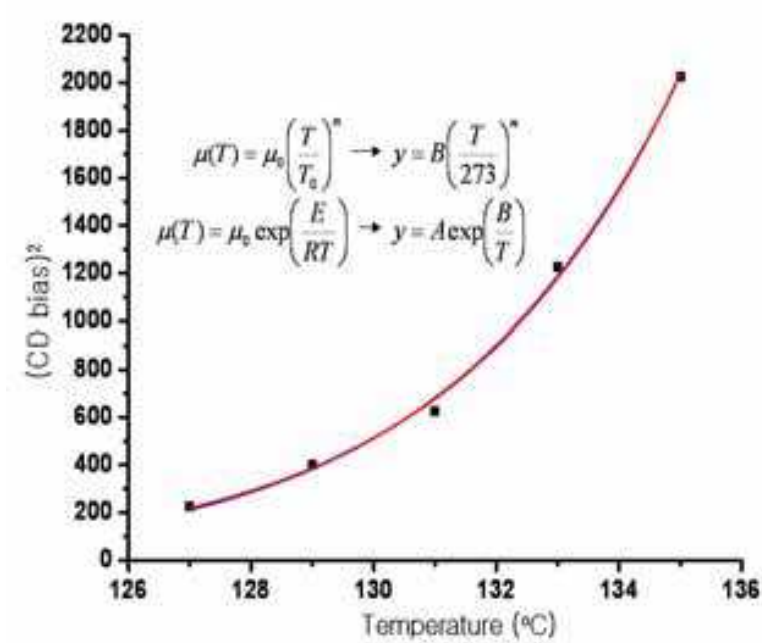
Fig. 5. Fitting experimental data by using viscosity equation of a function of temperature.

Figure 5 shows the experimental relation of temperature and the viscosity, which is from Eq. (19),

$$L^2 = \frac{t}{\rho} \mu \quad \rightarrow \quad \mu(T) \propto (CD\,bias)^2 \cdot \tag{21}$$

Two equations are fitted when A=3.0062×10^14, n=36.52117, A=7.5727×10^18, and B=-4840.2. Hence, two functions can be used as the viscosity function.
The function of viscosity can be

$$\mu(T) = \mu_0 \exp\left(\frac{E}{RT}\right), \tag{22}$$

- **Mask Pattern**
  140-nm × 140-nm isolated rectangle pattern
- **Modeling Options**
  Image Calculation Model: Scalar
- **Stepper Parameters**
  Illumination: Convential-partially coherent
  Defocus: 0.0-μm,   Wavelength: 193-nm
  Illumination Pupil Shape: Dipole (radius: 0.5, hole size: 0.3, angle: 45°)
  Numerical Aperture (NA): 0.7, Aberrations: none
  Flare[%]: 0
- **Film Stack**
  Layer 1: 250-nm resist, refraction : 1.72 - j0.02
  Layer 2: 82-nm AR^{TM}19, refraction : 1.79 - j0.4
  Layer 3: Silicon, refraction : 6.522 - j2.705
- **Prebake Parameters**
  Temperature: 120°C
  Time: 60 s
- **Exposure Parameters**
  Exposure Dose: 19 mJ/ cm^2
  A: 0.01 (1/ μm), B: 0.08 (1/ μm), C: 0.02-cm^2/ mJ
- **Post-Exposure Bake Parameters**
  Diffusion Length: 0.035-μm
  Time: 80 s,   Q: 0.067
  k_{amp} (1/ s): 0.75, k_{loss} (1/ s): 2.3x10^{-5}
  Resist Type: Positive
  Exponent n: 1
  Resist thickness reduction parameter: alpha: 1.74, beta: 0.02
  Activation Energy E_2: 0 eV
- **Develop Parameters**   Development Model: Enhanced Mack
  Time: 150 s,
  R_{min}: 6.5x10^{-5}-nm/ s R_{max}: 0.1-μm/ s
  R_{Res}: 0.0187   n: 0.01   l: 0.73
- **Resist Reflow Parameters**
  Temperature: 129°C,   Time: 90 s

Table III. Parameters of the 140-nm contact hole pattern after resist reflow.

where E is the activation energy, μ_o is the pre-exponential factor, and R is the universal gas constant. A fitted viscosity function, $\mu = (4.8414 \times 10^{16}) \bullet \exp(- 4840.2 / T)$, is used for the simulation when the density is constant due to temperature.

Table III shows the simulated parameters of the 140-nm contact hole after resist flow. A 140-nm mask pattern is used for the profile of a 180-nm C/ H pattern after the development process. After the resist flow process of 129 °C for 90 seconds, the 180-nm developed profile is shrunk to the 140-nm resist profile.

Figure 6 shows the simulated and experimental resist profiles after resist flow at 129 °C and 90 seconds. The critical dimension bias is 40 nm. The bulk image of simulation modeled by Eqs

(21) and (22) is shown as similar to the experimental bulk image. Figure 6 shows the comparison of CDs and CD biases after resist flow at 90 seconds in experiment and simulation according to temperature. Our simulated results agree well with experimental results.
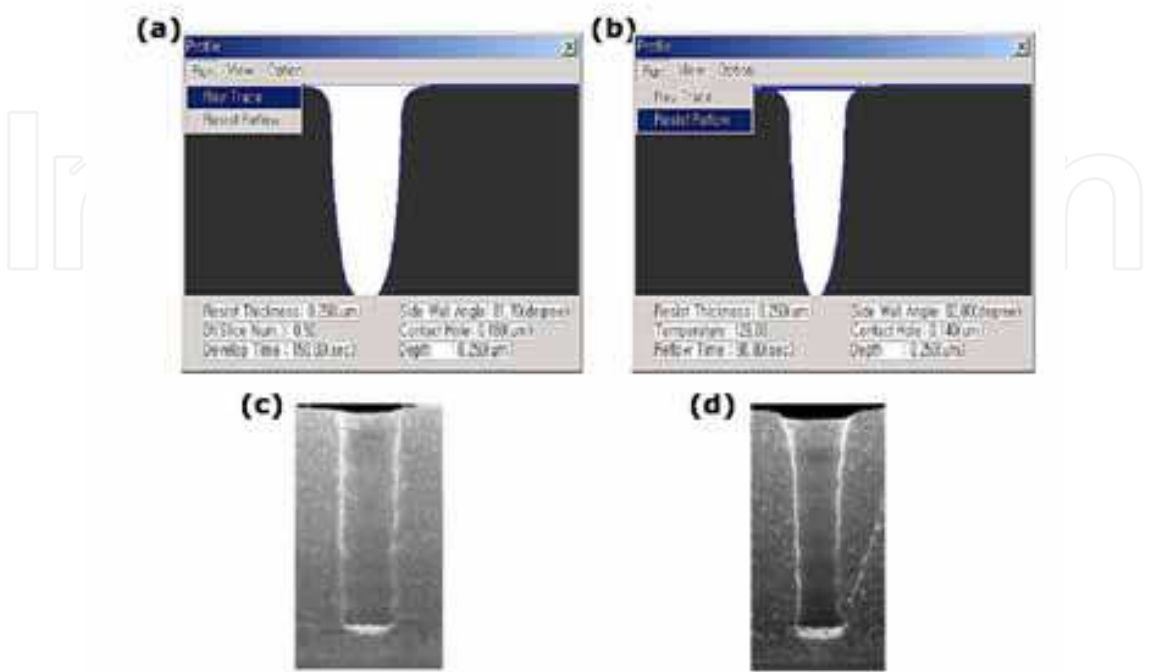

Fig. 6. Simulation results of (a) a 180-nm contact hole pattern before resist reflow, and (b) a 140-nm contact hole after resist reflow. Experimental results of (c) 180-nm contact hole pattern before resist reflow, and (d) 140-nm contact hole pattern after the resist reflow process.
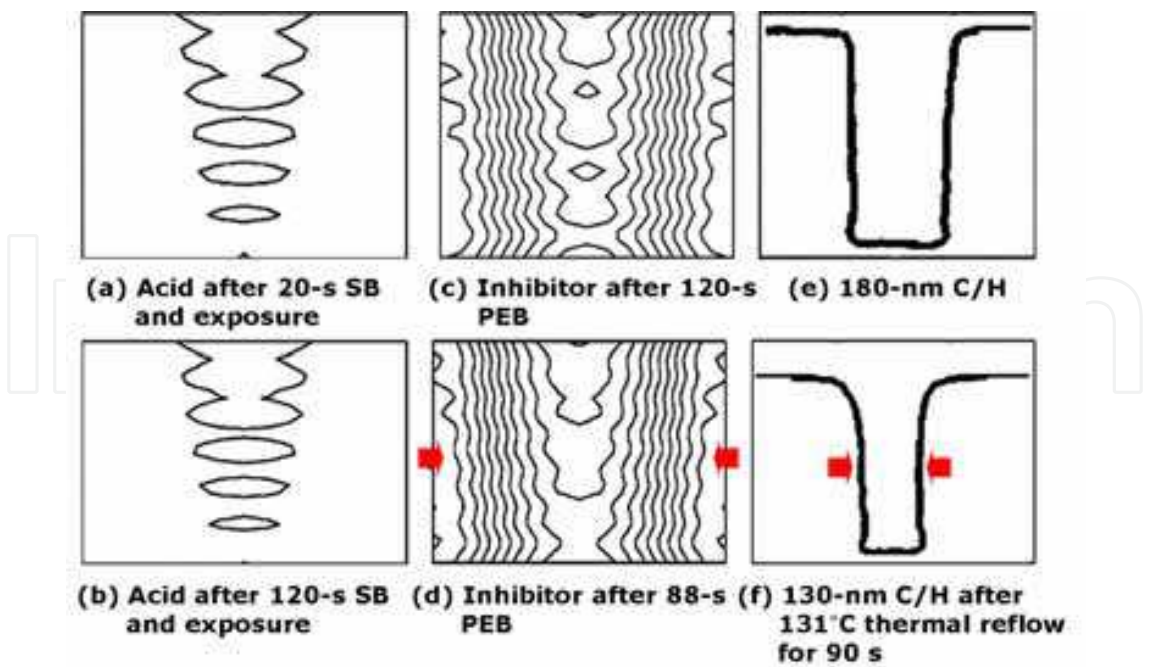
Fig. 7. Resist bulk images of acid concentration after exposure at SB times of (a) 20 s and (b) 120 s, inhibitor concentrations at PEB times of (c) 120 s and (d) 88 s, (e) the 180-nm contact hole before thermal reflow, and (f) the 130-nm contact hole after thermal reflow at 131 °C for 90 s.

Figure 7 shows boundary movements for a C/ H in SB, PEB, and thermal reflow. These resist bulk images are the distributions of acid concentrations after exposure at a SB time of 20 s in Fig. 7 (a) and at a SB time of 120 s in Fig. 7 (b). Figures 7 (c) and (d) show inhibitor concentrations at PEB times of 120 s and 88 s, respectively. Figures 7 (e) and (f) show the 180-nm C/ H before thermal reflow and the 130-nm C/ H after thermal reflow, respectively, at 131 °C for 90 s. For the extended SB time, the boundaries of the acid concentration are same in Figs. 7 (a) and (b), so the SB time is not sensitive to shrinkage of the contact hole. For the extended PEB time, the boundaries of the inhibitor concentration move to the center of the horizontal axis, and become dense. During the thermal reflow in Figs. 7 (e) and (f), the boundary of the C/ H shrinks due to temperature and time.

2.4.2 Solution of the Navier-Stokes equation

The resist reflow at temperature above its glass transition temperature can be assumed to be an ideal fluid, which is an incompressible fluid, and to have a constant density (ρ) and force ($\rho \hat{n} \delta S$) exerted across a geometrical surface element $\hat{n} \delta S$ within the fluid. Hence,

$$\frac{D\vec{u}}{Dt} = -\frac{1}{\rho}\nabla P + g , \quad \nabla \bullet \vec{u} = 0 , \tag{23}$$

where $\vec{u}(u,\phi,w)$ is the fluid velocity, g is the gravitational acceleration, ρ is the density, and P is the pressure. At this point, the element of the stress tensor (T_{ij}) in an incompressible fluid is

$$T_{ij} = -p\delta_{ij} + \mu\left(\frac{\partial u_j}{\partial x_i} + \frac{\partial u_i}{\partial x_j}\right), \quad \nabla \bullet \vec{u} = 0 . \tag{24}$$

where μ is fluid viscosity. By Eqs. (23) and (24),

$$\rho\frac{Du_i}{Dt} = -\frac{\partial P}{\partial x_i} + \mu\frac{\partial}{\partial x_j}\left(\frac{\partial u_j}{\partial x_i} + \frac{\partial u_i}{\partial x_j}\right) + \rho g_i , \tag{25}$$

$$\frac{Df}{Dt} = \frac{\partial f}{\partial t} + u\frac{\partial f}{\partial x} + v\frac{\partial f}{\partial y} + w\frac{\partial f}{\partial z} \rightarrow \frac{Df}{Dt} = \frac{\partial f}{\partial t} + (\vec{u} \bullet \nabla)f \cdot \tag{26}$$

Hence, the Navier-Stokes equation is

$$\frac{\partial \vec{u}}{\partial t} + (\vec{u} \bullet \nabla)\vec{u} = -\frac{1}{\rho}\nabla P + v\nabla^2\vec{u} + g , \tag{27}$$

$$\nabla \bullet \vec{u} = 0 , \tag{28}$$

where $v = \mu/\rho$ is kintic viscosity. In the x and the z directions,

$$\rho\left(\frac{\partial u}{\partial t} + u\frac{\partial u}{\partial x} + w\frac{\partial u}{\partial z}\right) = -\frac{\partial P}{\partial x} + \mu\left(\frac{\partial^2}{\partial x^2} + \frac{\partial^2}{\partial z^2}\right)u + \rho g_x , \tag{29}$$

$$\rho\left(\frac{\partial w}{\partial t} + u\frac{\partial w}{\partial x} + w\frac{\partial w}{\partial z}\right) = -\frac{\partial P}{\partial z} + \mu\left(\frac{\partial^2}{\partial x^2} + \frac{\partial^2}{\partial z^2}\right)w + \rho g_z, \tag{30}$$

$$\frac{\partial u}{\partial x} + \frac{\partial w}{\partial z} = 0 \cdot \tag{31}$$

When $\vec{u} \bullet \nabla \vec{u} \langle\langle \mu\nabla^2\vec{u}$ for the slow flow equation and when the gravitational acceleration (g_x) and pressure are neglected, the Navier-Stokes equation becomes the diffusion equations

$$\frac{\partial H}{\partial t} = v\frac{\partial^2 H}{\partial x^2}, \quad \text{if } u \approx H(x,t), \tag{32}$$

where H is a geometric boundary. In the shallow-water approximation, the Navier-Stokes equation becomes

$$\frac{\partial u}{\partial t} + u\frac{\partial u}{\partial x} + w\frac{\partial u}{\partial z} = -\frac{1}{\rho}\frac{\partial P}{\partial x}, \tag{33}$$

$$\frac{\partial w}{\partial t} + u\frac{\partial w}{\partial x} + w\frac{\partial w}{\partial z} = -\frac{1}{\rho}\frac{\partial P}{\partial z} - g_z, \tag{34}$$

$$\frac{\partial u}{\partial x} + \frac{\partial w}{\partial z} = 0 \cdot \tag{35}$$

From Eq. (35),

$$w = -\frac{\partial u}{\partial x}z + f(x,t) \tag{36}$$

and $f(x, t) = 0$ when w = 0 at z = 0. If $F(x, z, t) = z - H(x, t)$ in the kinematic condition at the free surface,

$$\frac{\partial F}{\partial t} + (\vec{u} \bullet \nabla)F = 0, \text{ at z = } H(x, t). \tag{37}$$

From Eqs. (36) and (37),

$$\frac{\partial H}{\partial t} + u\frac{\partial H}{\partial x} + H\frac{\partial u}{\partial x} = 0 \cdot \tag{38}$$

By using $c(x,t) = (gH)^{\frac{1}{2}}$ and Eq. (33),

$$\left[\frac{\partial}{\partial t} + (u-c)\frac{\partial}{\partial x}\right](u-2c) = 0 \cdot \tag{39}$$

When $u + 2c = 2c_0$, $z = -3c + 2c_0$, and $z \approx c \approx H(x,t)$,

$$\frac{\partial H}{\partial t} + H\frac{\partial H}{\partial x} = 0 \cdot \tag{40}$$

For an analytical solution, the gravitational acceleration (g_x) in the x-direction is zero and $\vec{u} \bullet \nabla \vec{u} \langle\langle \mu \nabla^2 \vec{u}$ for the slow flow equations. From Eq. (29),

$$0 = -\frac{1}{\rho}\frac{\partial P}{\partial x} + v\frac{\partial^2 u}{\partial z^2} \quad \text{for x-coordinate,} \tag{41}$$

where kinetic viscosity is $v = \mu / \rho$. From Eq. (30),

$$0 = -\frac{1}{\rho}\frac{\partial P}{\partial z} - g \quad \text{for z-coordinate.} \tag{42}$$

The net upward force per unit area of surface is, by Eq. (41),

$$P - P_0 = -\Im\frac{\partial^2 H}{\partial x^2} \rightarrow P = -\rho g H - \Im\frac{\partial^2 H}{\partial x^2} , \tag{43}$$

where P is the pressure in the fluid just below the surface, P_0 is the atmospheric pressure, and $\Im$ is the surface tension force. If the geometric boundary function (H) is a power series, $H = 1 + x + x^2 + \cdots$ and if x is smaller then 1, $H \approx 1 + x$ and

$$P = -\rho g(1 + x) - \Im\frac{\partial^2 H}{\partial x^2} . \tag{44}$$

From Eqs. (41) and (44),

$$u = -\left[\frac{g}{v}\frac{\partial H}{\partial x} + \frac{\Im}{v\rho}\frac{\partial^3 H}{\partial x^3}\right]\frac{1}{2}z^2 . \tag{45}$$

From Eq. (31),

$$w_{z=H} = \frac{\partial}{\partial x}\left[\frac{g}{v}\frac{\partial H}{\partial x} + \frac{\Im}{v\rho}\frac{\partial^3 H}{\partial x^3}\right]\frac{1}{6}H^3 . \tag{46}$$

The boundary condition is $F(x,z,t) = z - H(x,t) = 0$, so that

$$\frac{\partial H}{\partial t} = \frac{\partial}{\partial x}\left[\frac{H^3}{6}\left(\frac{g}{v} + \frac{\Im}{v\rho}\frac{\partial^3 H}{\partial x^3}\right)\right], \tag{47}$$

$$\frac{\partial H}{\partial \tau} = \frac{1}{6}\frac{\partial}{\partial X}\left[\Omega^{-2}\left(\frac{\partial^3 H}{\partial X^3}\right)H^3 + H^3\right], \quad X \equiv \frac{x}{w}, \quad \tau \equiv \frac{gt}{wv}, \quad \Omega^2 \equiv \frac{\rho g w^3}{\Im}, \tag{48}$$

where H is the film geometry, w is the feature width, v is the kinematic viscosity of the fluid, and $\Im$ is the surface tension. A quasi-steady state of resist reflow can be obtained by dropping $\partial H / \partial \tau$ from Eq. (48):

$$\left(\frac{\partial^3 H}{\partial X^3}\right)H^3 + \Omega^2 H^3 = \Omega^2 . \tag{49}$$

Analytical solutions with the dimensionless parameter (Ω^2) can be obtained. In the isolated contact hole, the entire domain can be divided into subdomain I of the left ridge side, subdomain II of the inside ridge, and subdomain III of the right ridge side. The film geometries are

$$H_I = 1 + b_1\phi_2 + c_1\phi_3, \quad H_{II} = 1 \pm \frac{d}{1+\Omega^2} + a_2\phi_1 + b_2\phi_2 + c_2\phi_3 + \phi_4, \quad H_{III} = 1 + a_3\phi_1, \quad (50)$$

where a, b, and c are coefficients, which are calculated by using the boundary conditions, d is the height of resist, and ϕ is the linearly independent homogenous solutions. The three linear independent homogenous solutions are

$$\phi_1 = \exp(-\lambda x), \quad \phi_2 = \exp(\lambda x/2)\cos(\lambda x\sqrt{3}/2),$$

$$\phi_3 = \exp(\lambda x/2)\sin(\lambda x\sqrt{3}/2), \quad \phi_4 = \frac{1}{3}\left[\left(1 \pm \frac{d}{1+\Omega^2}\right) - \left(1 \pm \frac{d}{1+\Omega^2}\right)^4\right], \quad (51)$$

where in subdomains I and III, $\lambda = (3\Omega^2)^{1/3}$ and , in subdomain II, $\lambda = \{3\Omega^2\{1 \pm d/(1+\Omega^2)\}^{-4}\}^{1/3}$. In the boundary condition of x = -1/2,

$$H_I \pm d = H_{II}, \quad \frac{\partial H_I}{\partial X} = \frac{\partial H_{II}}{\partial X}, \quad \frac{\partial^2 H_I}{\partial X^2} = \frac{\partial^2 H_{II}}{\partial X^2}. \quad (52)$$

In the boundary condition of x = 1/2,

$$H_{III} \pm d = H_{II}, \quad \frac{\partial H_{III}}{\partial X} = \frac{\partial H_{II}}{\partial X}, \quad \frac{\partial^2 H_{III}}{\partial X^2} = \frac{\partial^2 H_{II}}{\partial X^2}. \quad (53)$$

If wafer has a topology, the thickness of resist after thermal reflow is different due to reflow conditions. The surface tension of resist varies due to the non-uniformity of resist thickness. In the dense contact holes, the film geometries are

$$H_I = 1 + \frac{d}{1+\Omega^2} + a_2\phi_1 + b_2\phi_2 + c_2\phi_3 + \phi_4, \quad (54)$$

$$H_{II} = 1 + a_2\phi_1 + b_2\phi_2 + c_2\phi_3. \quad (55)$$

The boundary conditions at x = 1/2 are

$$H_I = H_{II} + d, \quad \frac{\partial H_I}{\partial X} = \frac{\partial H_{II}}{\partial X}, \quad \frac{\partial^2 H_I}{\partial X^2} = \frac{\partial^2 H_{II}}{\partial X^2}. \quad (56)$$

The boundary conditions between x = -1/2 and x = a + 1/2 are

$$H_{II(X=z+1/2)} + d = H_{I(X=-1/2)}, \quad \frac{\partial H_I}{\partial X_{(X=-1/2)}} = \frac{\partial H_{II}}{\partial X_{(X=a+1/2)}}, \quad \frac{\partial^2 H_I}{\partial X^2}_{X=-1/2} = \frac{\partial^2 H_{II}}{\partial X^2}_{(X=a+1/2)}. \quad (57)$$

Figure 8 shows the numerical result of the diffusion equation in Eq. (32). The isolated pattern is wide and symmetrical due to the time of thermal reflow. The numerical

calculation methods are the second predictor-corrector scheme, quick scheme, the forward time and centered space (FTCS) scheme, and the Kawamara-Kuwahara scheme.
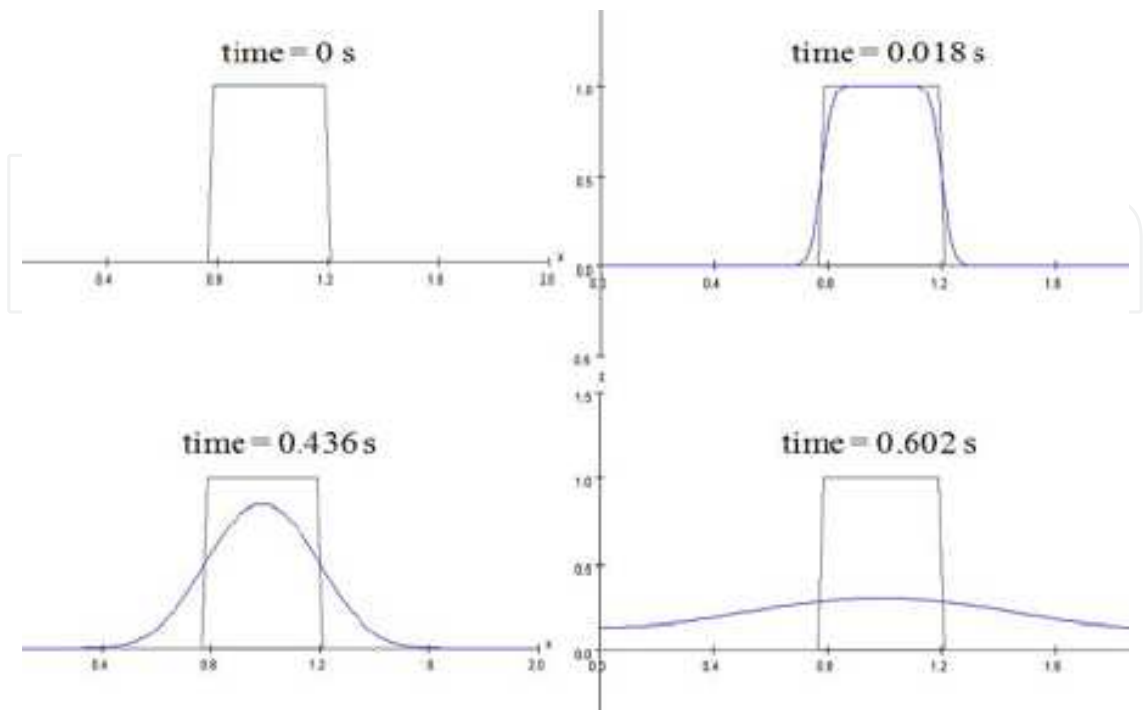

Fig. 8. Simulation results of the diffusion equation in Eq. (32) by using are the second predictor-corrector scheme, quick scheme. The isolated pattern is wider and symmetrical due to the time of thermal reflow.
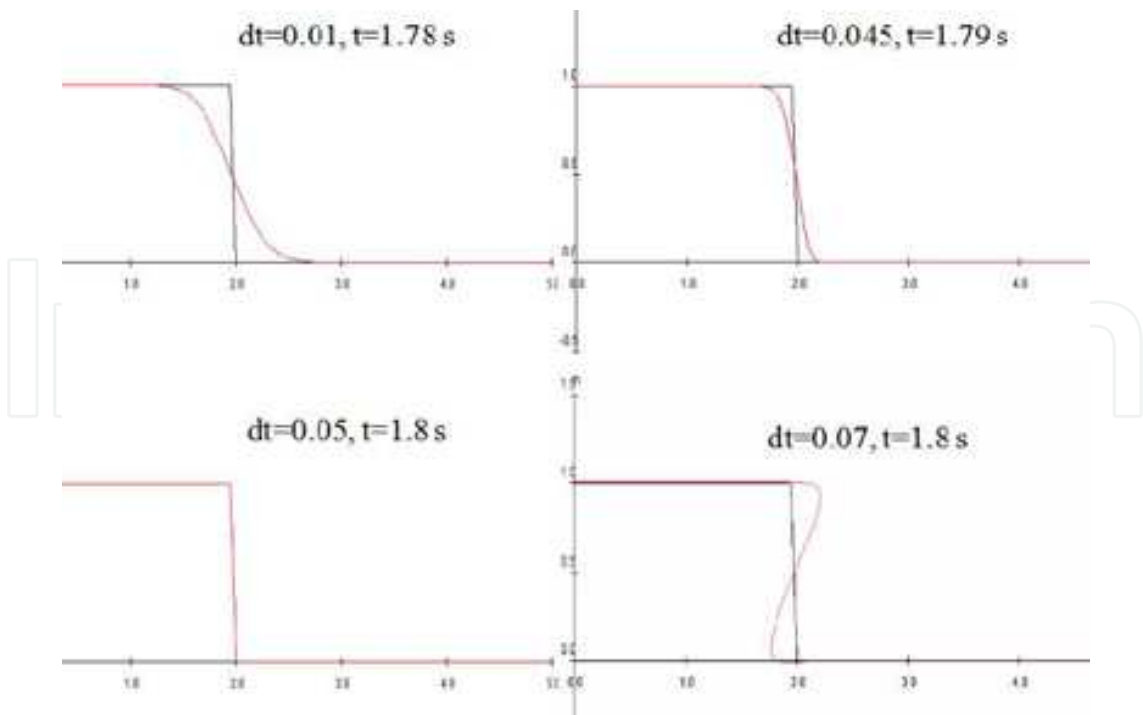

Fig. 9. Simulation flow of Eq. (40) due to Δt of the courant number, which is reflow time interval.

Figure 9 shows pattern reflow due to Δt of the courant number, which is reflow time interval in Eq. (40). As this time interval is larger, pattern side forms the slop of h = - x, a vertical slop, and the slop of h = x. These results are same as experiment results. It can be assumed that the temperature of thermal reflow makes molecular of resist moving, this high temperature corresponds to the large time interval, which is rapid reflow. The numerical calculation methods are the upstream scheme and Lax-Wendroff scheme.
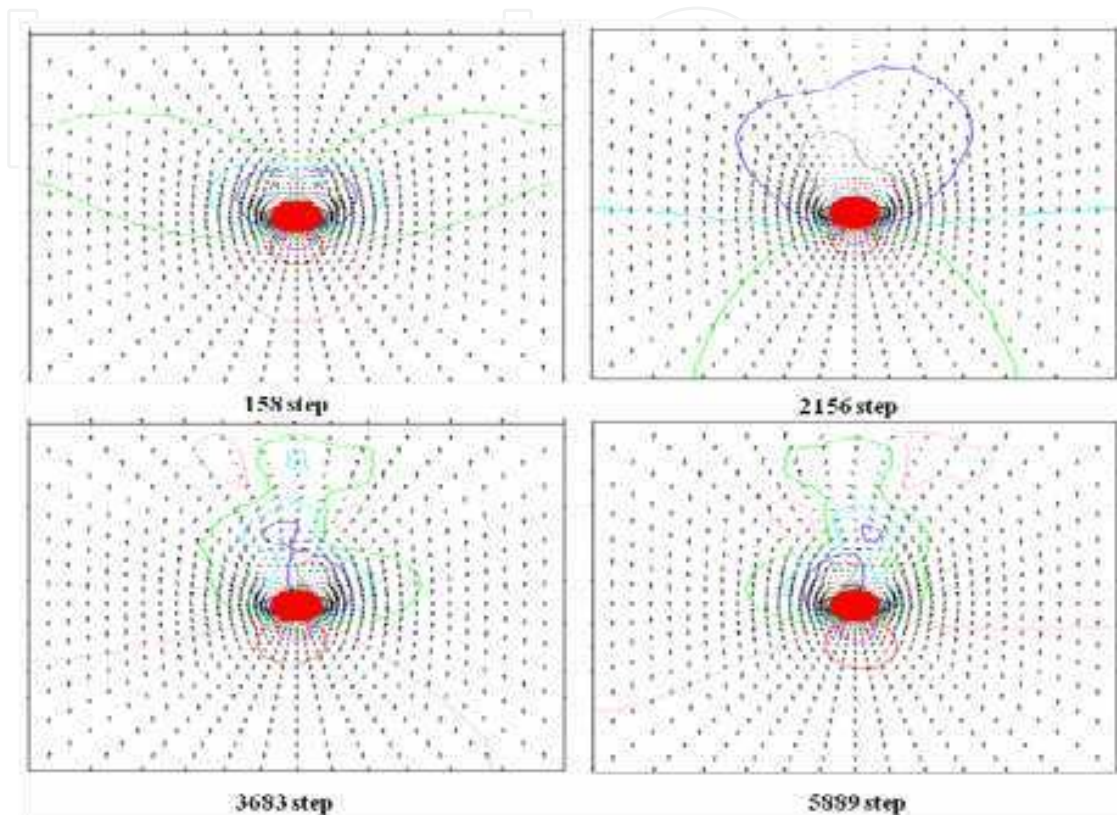
Fig. 10. Reflow velocity and pressure distributions in Eqs (29-31) by using a finite element method. These results are obtained by modifying the simulation of Prof. Tomomi Uchiyama in Nagoya University, Japan.

Figure 10 shows the reflow velocity and pressure distributions of Eqs (29-31) without the gravitational acceleration by using a finite element method. These results are obtained by modifying the simulation of Prof. Tomomi Uchiyama in Nagoya University, Japan. The boundary conditions are $v_i = \bar{v}_i$ on bottom, left, and right sides, and $\left(-p/\rho\delta_{ij}+v\partial v_i/\partial x_j\right)n_j = \bar{t}_i$ on top side where t is surface tension. In Fig. 10, the step is corresponding to the time of thermal reflow, reflow velocity is described as an arrow, and pressure is described as contour in the two dimensions. Due to steps, various velocity directions and pressure contours are shown in Fig. 10.

Figures 11 (a)-(c) show wet profiles of thermal reflow according to the parameter Ω in Eq. (49). The simulation parameters are resist thickness (μm) = 0.1 and trench width (μm) = 0.1. The larger the dimensionless parameter ($\Omega_1^2 = 7.54 < \Omega_2^2 = 426.09 < \Omega_3^2 = 7538.46$, which are surface tension $\Im_3 < \Im_2 < \Im_1$ due to Eq. (48)) is, the sharper the slope of trench area is. Figure 11 (d) shows the SEM digitization lines due to the temperature of the resist reflow process [6]. The higher the temperature is, $T_3 < T_2$, the shaper the corner edges of resist

profile are. These corners become round and collapse at temperature above T_1 ($> T_2$). Surface tension is the magnitude of the force that is a force of attraction between molecules in liquids and controls the shape of the liquid. When temperature is increased, the surface tension is reduced because the attractive force between molecules in liquids is decreased, and density is reduced. As the change of density is larger than that of surface tension due to temperature, the simulation results of the dimensionless parameters ($\Omega_1 < \Omega_2 < \Omega_3$) in Fig. 11 (a-c) can be described the simulation results of temperatures ($T_1' > T_2' > T_3'$). The simulation results of temperatures can be described the geometry boundary movements of the experimental results in temperatures ($T_1 > T_2$). In comparison with experiment in Fig. 11 (d), the simulation result is for a quasi-steady-state and a wet resist state of resist reflow, so that this result excludes time dependency and the evaporation of resist materials.
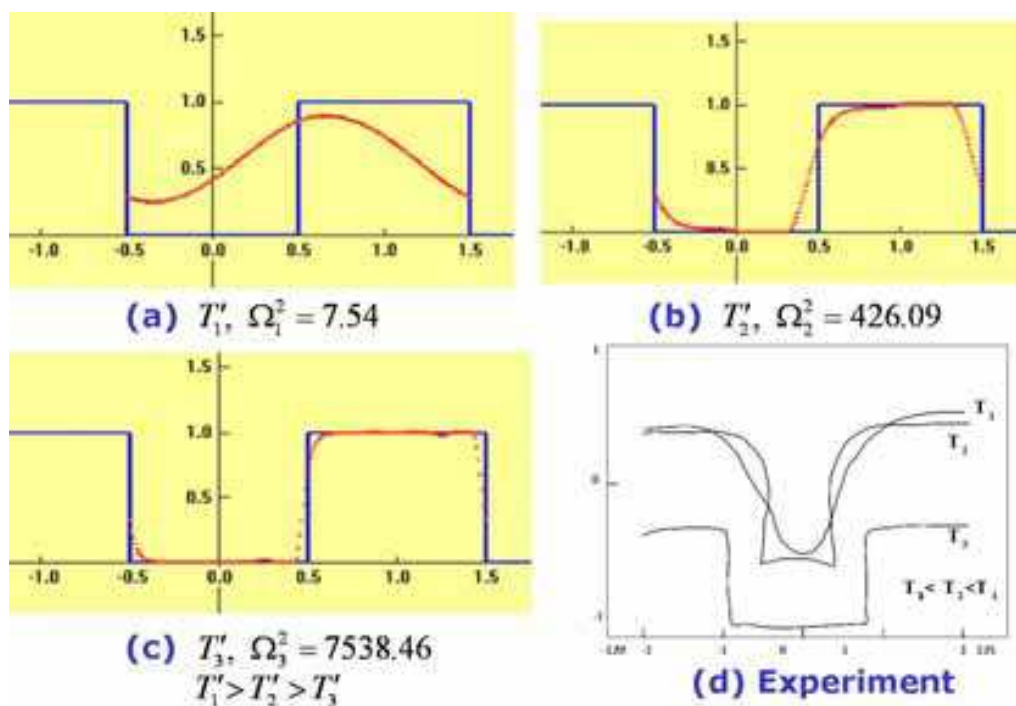
Fig. 11. Simulation results of (a) wet thermal reflow Ω_1, (b) wet thermal reflow Ω_2, (c) wet thermal reflow Ω_3, and (d) SEM digitization [6].

3. Thermal bias

During lithography process, image distortion is produced. Intensity distribution from the exposure system is different due to pattern size, wavelength, and illumination condition. Figure 12 shows the simulated optical process effects of the line and space (L/ S) patterns and contact hole (C/ H) patterns. The simulated resists of Figs. 12 (a) and (b) are V2 Shipley [7] and XP-99185 Shipley [8] respectively. The dose parameter is only controlled to get a L/ S pattern with 80° side wall angle in V2 Shipley and a C/ H pattern with 89.5° side wall angle in XP-99185 Shipley. In case of L/ S patterns in Fig. 12 (a), a similar increased behavior in both conventional illumination and annular illumination is shown according to pitch size. However, it is not enough to decide this behavior. In case of C/ H patterns in Fig. 12 (b), it is hard to find symmetric OPE effects for C/ H patterns in annular and conventional

illuminations. OPE effects of C/H patterns are more random than OPE effects of L/S patterns. OPE effects according to pitch size are differently depended on illumination conditions, pattern shapes, and mask size.
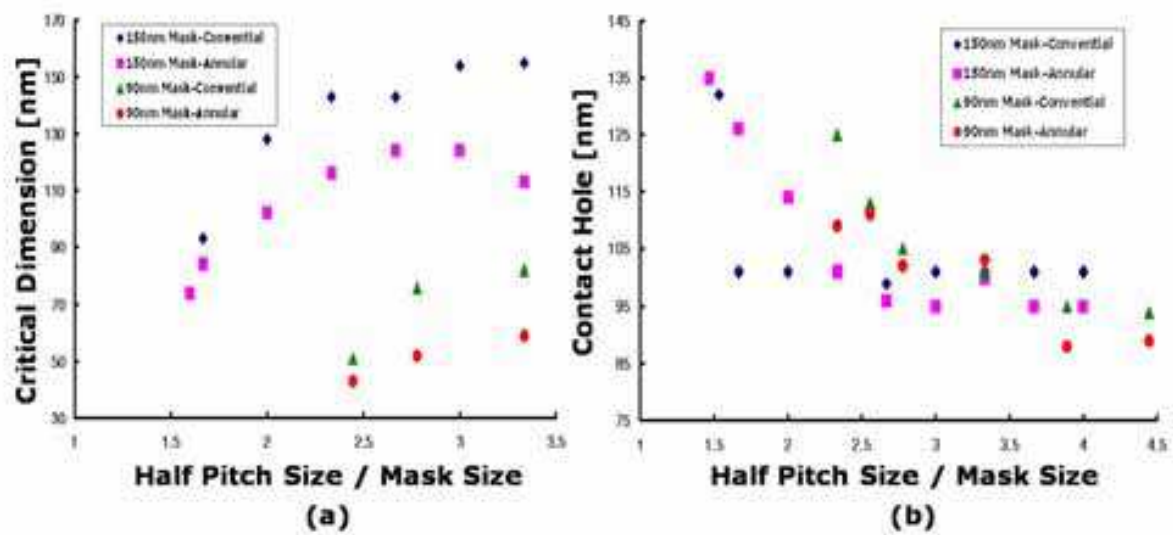

Fig. 12. Simulated optical process effects: (a) the graph between critical dimension and the ratio of haft pitch size and mask size at the L/S patterns and (b) the graph between contact hole and the ratio of half pitch size and mask size at the C/H patterns due to different mask size and illumination conditions.

Figure 13 shows the simulation results for the dependence of the size of the C/H on the pitch size for various PEB times and thermal reflow. Due to pitch size, C/H patterns between 140 nm and 114 nm are shaped in the solid line of Fig. 13 with triangle points by using a 140 nm mask and a PEB time of 100 s. These patterns, which depend on pitch size, can be reduced to C/H patterns between 97 nm and 43 nm in the dotted line of Fig. 13 with circle points by using a PEB time of 94 s and a thermal reflow of 138 °C. However, the optical proximity effects (OPE) are severe in Fig. 13.
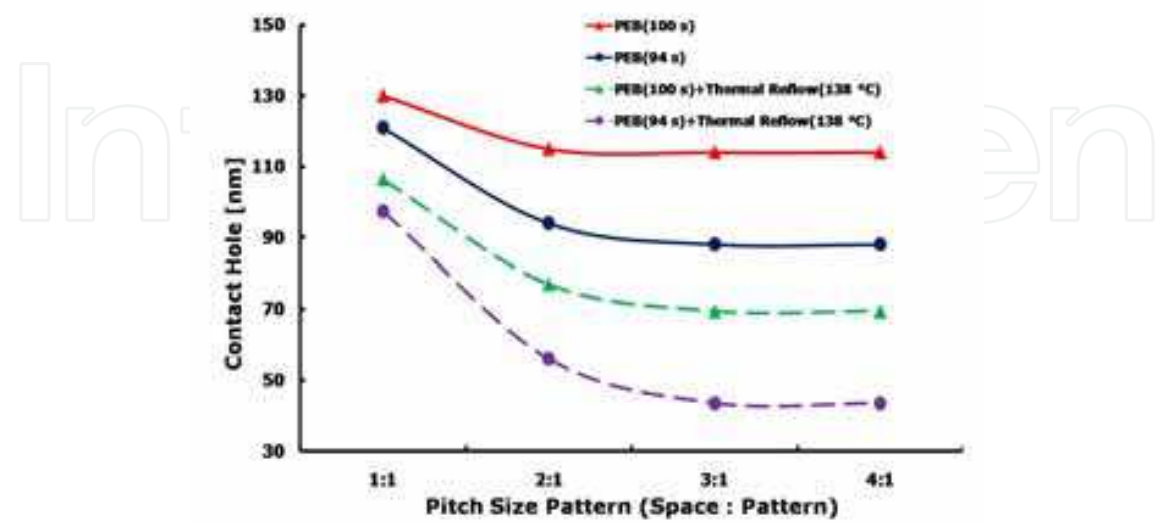
Fig. 13. Simulation results showing the dependence of the size of the contact hole on the pitch size for various PEB times and thermal reflow.

During the lithography process, image distortion is produced. The intensity distribution from the exposure system is different due to pattern size, wavelength, and illumination conditions. In the lithography process including thermal reflow, the MEEF can be divided into the MEEF after development and the MEEF after thermal reflow:

$$MEEF = \left[MEEF\right]_{develop} \bullet \left[MEEF\right]_{thermal} , \tag{58}$$

$$\frac{\Delta CD_{wafer}}{\Delta CD_{mask} / M} = \left[\frac{\Delta CD_{develop}}{\Delta CD_{mask} / M}\right]_{develop} \bullet \left[\frac{\Delta CD_{wafer}}{\Delta CD_{develop}}\right]_{thermal} , \tag{59}$$

where M is the imaging reduction ratio. The MEEF after development means the MEEF before thermal reflow.
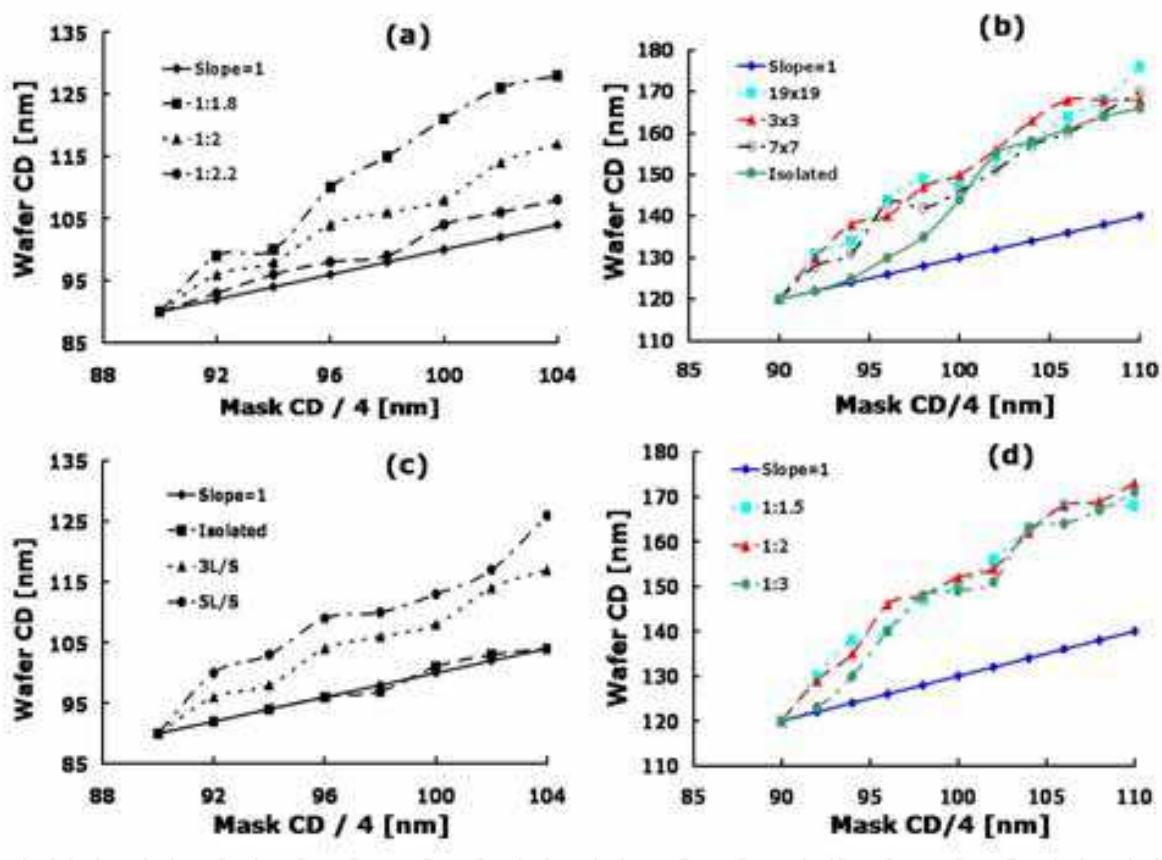
Fig. 14. Simulated MEEF after development for optical process effects: (a) MEEF due to the L/ S pattern density, (b) MEEF due to the C/ H pattern density, (c) MEEF due to the L/ S pitch size, and (d) MEEF of the C/ H pitch size.

Figure 14 shows the simulated optical process effects of the line and space (L/ S) patterns and the C/ H patterns. The simulated resists are the V2 Shipley resist [7] for L/ S patterns and the XP-99185 Shipley resist [8] for C/ H patterns. The dose parameter is only controlled to get a L/ S pattern with an 88° side wall angle for the V2 Shipley resist and a C/ H pattern with an 89.5° side wall angle for the XP-99185 Shipley resist. For a target 90-nm critical dimension, the MEEF value is large for the dense 1:1.8 pattern, and the MEEF value is approximately 1 for the isolated line in Fig. 14 (a). When the pitch is smaller in Fig. 14 (c),

the MEEF value is larger, and the pattern is difficult to form. For a 90-nm contact hole, the MEEF factors after development are not much different due to the pattern density of contact hole in Fig. 14 (b). However, variations of these OPEs with the pattern density is not symmetric. When the pitch of a 3 x 3 C/ H pattern is smaller, the MEEF after development is larger in Fig. 14 (d). The OPEs of C/ H patterns are more random than the OPEs of L/ S patterns. The higher-order MEEF factors are the MEEF of the C/ H, the L/ S, and the isolated patterns. The OPEs very with the line number and the pitch size for L/ S and contact-hole patterns. Hence, different OPC methods are needed for those patterns.
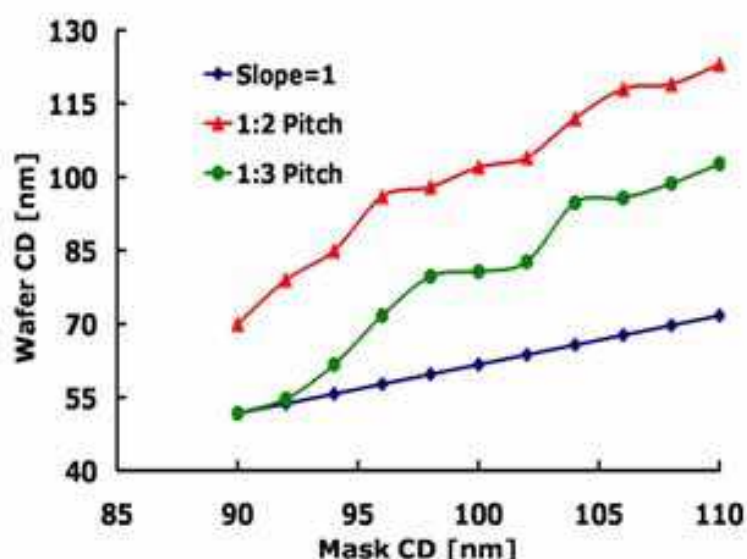
Fig. 15. Simulated MEEF of the contact hole after thermal reflow due to pitch size.

Figure 15 shows the simulated MEEF factors after thermal reflow for contact holes. The MEEF factors after thermal reflow at 140 °C are different due to pitch size in Fig. 15. Thus, different OPC methods must be applied for temperature and pitch size.

Thermal bias means the reduction of CDs before and after thermal processes. SB is a thermal process before exposure. During SB, the reduction of the free volume content in CAR significantly affects its lithographic properties. When CAR is exposed to the light, acid is generated by conversion of the photoactive generator. During a subsequent PEB, the photogenerated acid catalyzes a thermally induced reaction that cleaves the dissolution inhibitor groups (protecting groups), rendering the reacted (deprotected) region soluble in aqueous developer. Meanwhile, the acid diffuses from a high dose region to a low dose region washing out standing waves and causing the reacted region to be larger than the initially exposed region. For SB and PEB, the function of thermal biases (CD$_{SB (or PEB)}$) can be represented as

$$\Delta CD_{SB(or\,PEB)} = CD_{T=T_{t\,\arg et}} - CD_T ,\tag{60}$$

where $CD_{T=T_{t\,\arg et}}$ is CD after development with SB (or PEB) at temperature T = T$_{target}$ and CD$_T$ is CD after development with SB (or PEB) at temperature T. Thermal reflow is an extra bake and chill step to reduce the pattern size of resist after the final images are developed. When resist is heated over its glass transition temperature, the bonding of synthesized resist is reduced and its mobility is improved. The three-dimensional structure of the synthesized

resist is changed, and C/ H is shrunk due to the additional thermal energy. For thermal reflow, the function of thermal bias can be represented as

$$\Delta CD_{\text{Thermal reflow}} = CD_{\text{dev}} - CD_{\text{wafer}}. \tag{61}$$

Those three kinds of thermal processes have similar effective parameters such as baking temperature (T_b), baking time (t_b), resist original characteristics (K_r), resist volume surrounding (V_R), initial pattern size and shape, and pattern array. For the simple thermal assumption, the actual thermal bias of each thermal process can be approximated as an orthogonal function,

$$\Delta CD = f\left(T_b, t_b, V_R, K_r\right) = f\left(T_b, t_b\right) \bullet f\left(V_R\right) \bullet f\left(K_r\right), \tag{62}$$

where $f(T_b, t_b)$ is a thermal bias due to temperature and time, $f(V_n)$ is a thermal bias due to resist volume surrounding C/ H, and $f(K_r)$ is a thermal bias due to resist characteristics.

4. Comparison to experiment results

By matching with experiment results [9], simulation conditions are optimized. For a 193 nm ArF CAR, 6% transmittance attenuated PSM, quaterpole off-axis illumination (OAI), ArF 193 nm illumination, 0.75 NA, 0.35 μm CAR thickness, and 0.082 μm BARC are used. For a 248 nm KrF CAR, 6% transmittance attenuated PSM, dipole OAI, KrF 248 nm illumination, and 0.8 NA are used. Photoresist (PR) type is SL120H, PR thickness is 0.45 μm, and BARC is 0.06 μm.

For thermal reflow, an antireflective layer of 80-nm-thick resist is coated over the silicon wafer prior to the resist process. The coated thickness is 0.37 μm. An ethylvinylether-based polymer is coated and prebaked at 100°C for 60 s. The exposure system is an ASML-700 with a numerical aperture (NA) of 0.6, a partial coherency (σ) of 0.4 and an attenuated phase-shift mask. Exposed wafers are baked at 110°C for 60 s on a hot plate and developed in 2.38 wt % tetramethyl ammonium hydroxide (TMAH) aqueous solution for 60 s. The time of resist reflow is 90 s.
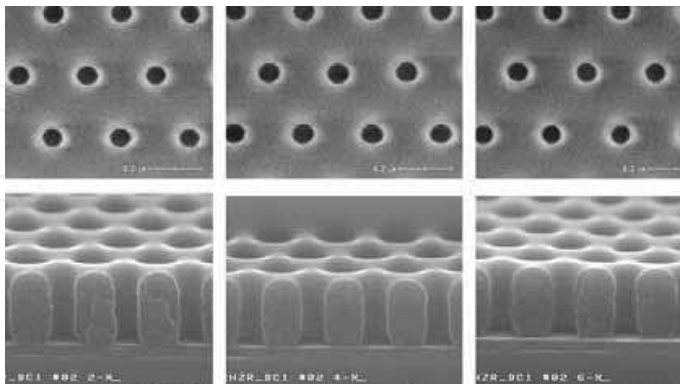

Fig. 16. SEM images of contact holes for various temperatures and duty ratios [9].

Figures 16 and 17 show experimental results of Hynix Semiconductor Inc. due to various temperature and duty ratios for KrF 248 nm [9] and ArF 193 nm illumination [10, 11]. The contact holes become smaller as the duty ratio becomes larger and as the temperature becomes larger.
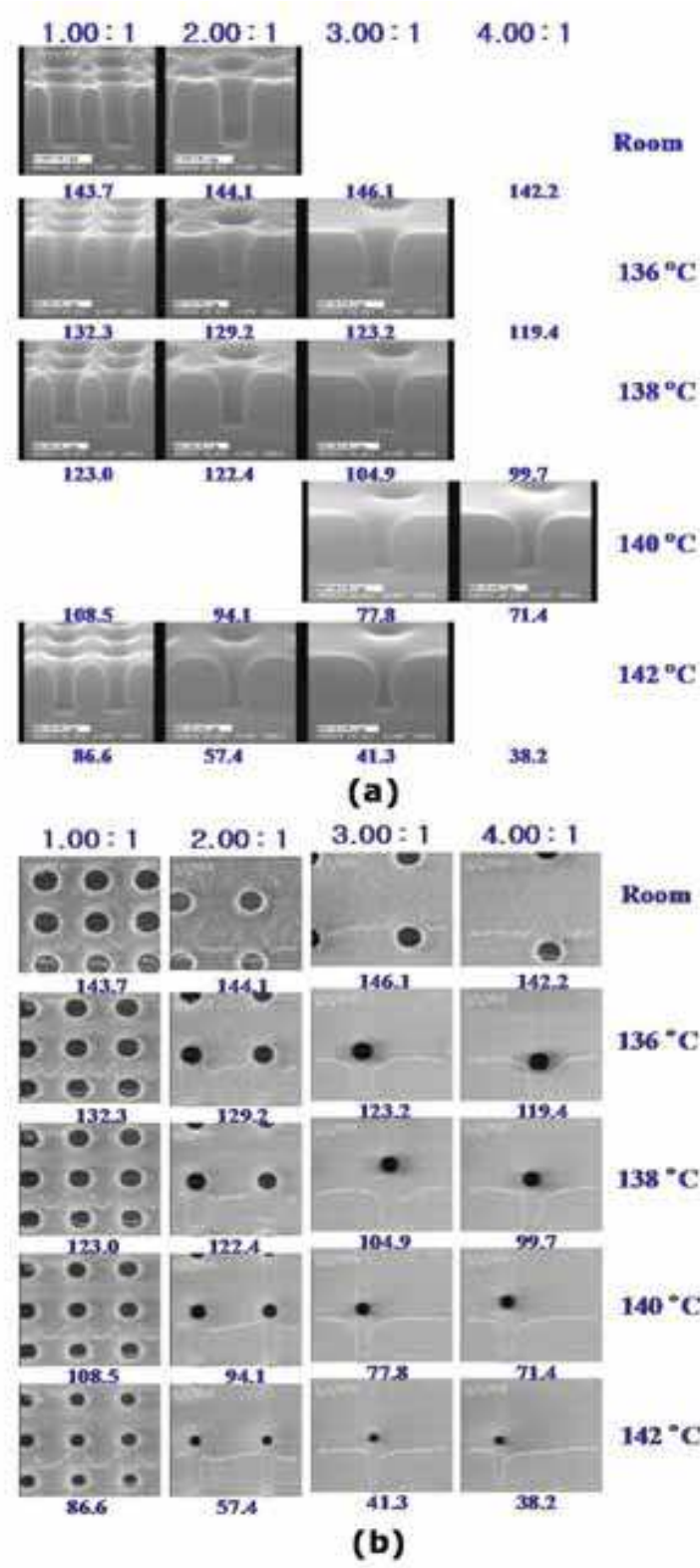
Fig. 17. Experimental results of (a) side view and (b) top view for various temperature and duty ratios in Hynix Semiconductor Inc. [10, 11]

Figure 18 shows simulation results of C/ H pattern shrinkages after thermal processes as a function of time for 248 nm KrF and 193 nm ArF CARs. Both of CARs have similar thermal

effects. The underbake PEB and the thermal reflow can reduce CD. However, during SB, CD is unchanged. During thermal reflow, CD is saturated quickly due to time. SB is soft bake, PEB is post exposure bake, and TR is thermal reflow.
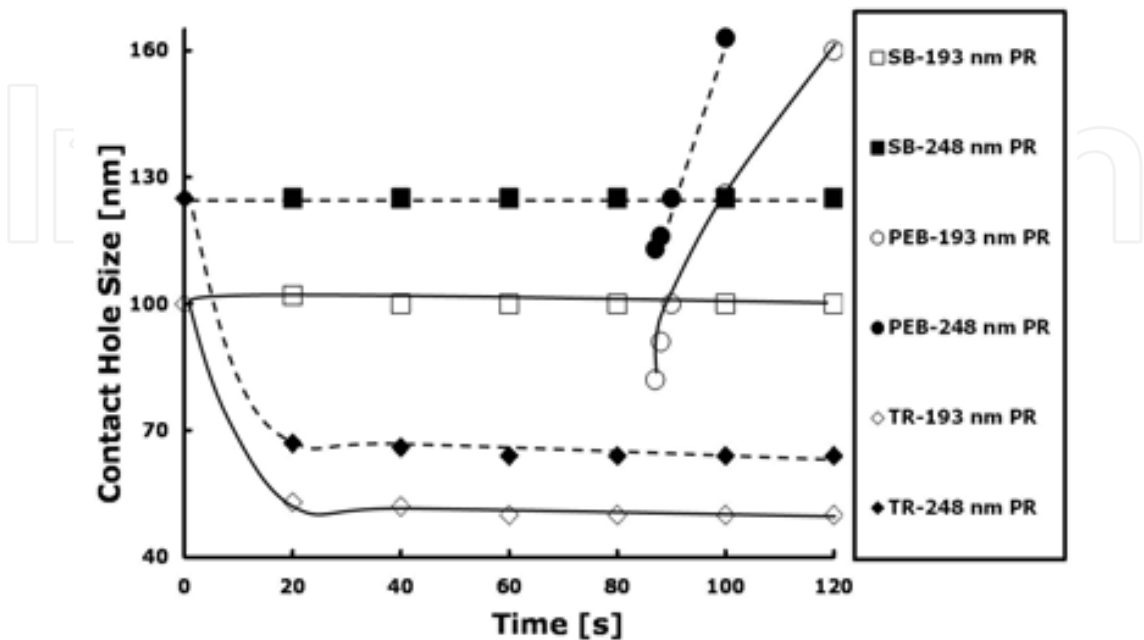
Fig. 18. Simulation results of pattern shrinkages after thermal processes as a function of time for ArF 193 nm and KrF 248 nm CARs.

	Thickness	CD sensitivity on temp.	CD sensitivity on time
Softbake	$d_y \approx \chi_S$	≈ 0.26 nm/ °C	≈ 0 nm/ s
PEB	$d_y \approx C_{as}$	≈ 3 nm/ °C	≈ 2.3 nm/ s
Thermal Reflow	$d_x = \sqrt{\dfrac{\mu}{\rho}}t$	≈ 10 nm/ °C	≈ 2.3 nm/ s

Table IV. Comparison of thermal processes (d_y: the thickness reduction in y-direction, d_x: the thickness reduction in x-direction, χ_S: the mass fraction of solvent, C_{as}: the concentration of deprotection resin, μ: the fluid viscosity, ρ: the density, t: the time, and temp.: the temperature)

Table IV shows simulation parameters with thickness variation of thermal processes, and the CD sensitivities of these process temperatures and times for a C/ H pattern. Among the thermal processes, thermal reflow is the most effective method for 45-nm pattern formation. The CD sensitivity of a C/ H pattern can be improved to 4.6 nm/ s by using the PEB time and thermal reflow. However, due to the pitch size, these thermal processes produce OPEs, such as the impact of the image distortion. The OPE is quite severe when those thermal process are used for 45-nm patterns, so model-based OPC must be performed.

Figure 19 shows simulation results for thermal SB bias. CD shrinkage is dependent on pitch sizes. Thermal SB biases are depended only on two kinds of pattern types such as isolated pattern and dense pattern:

$$f^2_{SB}(V) \approx f^2_{SB}(R) = \begin{cases} 1 & \textit{for isolated pattern} \\ \alpha_1 & \textit{for dense patterns} \end{cases} \tag{63}$$

where R is the ratio of contact hole and half pitch size and α_1 is a constant value. The thermal PEB bias of pitch size includes thermal SB bias because PEB process is a following process after SB process: $f_{SB}(R) \leq f_{PEB}(R)$. A 193 nm resist has larger thermal bias than a 248 nm resist in Fig. 19.
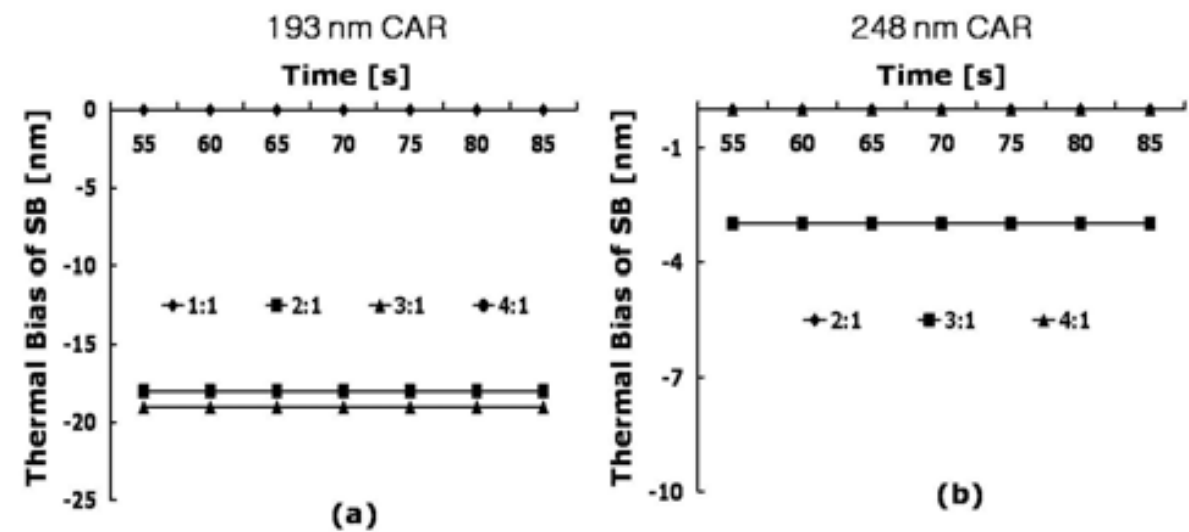

Fig. 19. Simulation result for thermal biases of SB. For both of a ArF 193 nm CAR in Fig. 19 (a) and a KrF 248 nm CAR in Fig. 19 (b), CD shrinkage is independent on SB time and SB temperature, but dependent on pitch sizes.
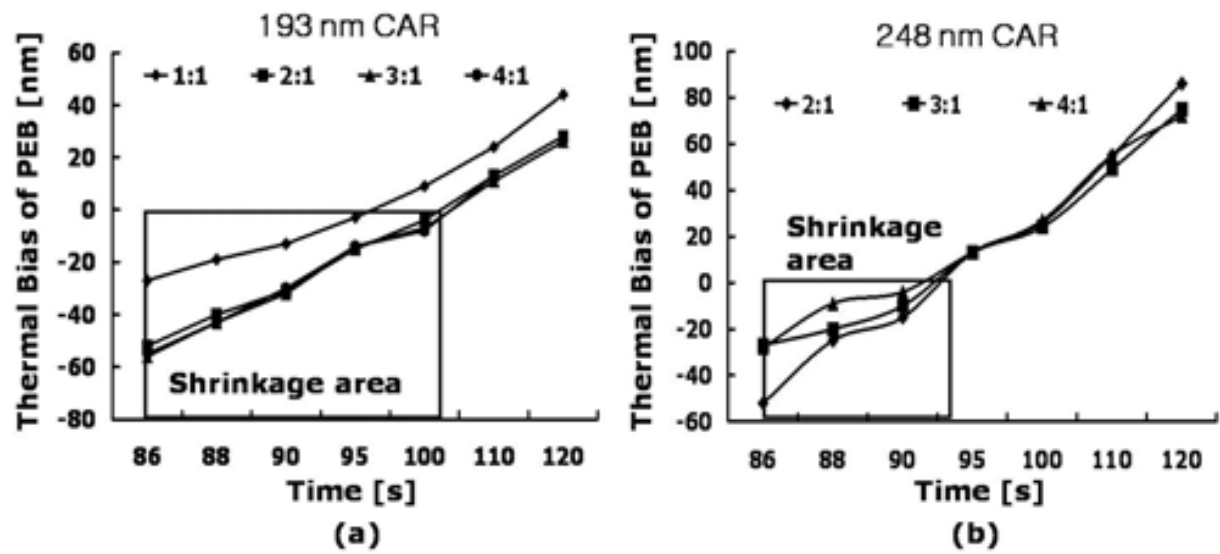
Fig. 20. Simulation results for thermal biases of PEB. In both of a ArF 193 nm CAR in Fig. 20 (a) and a KrF 248 nm CAR in Fig. 20 (b), the C/ H pattern of 1:1 line and space has different PEB effects with other C/ H patterns

Figure 20 shows simulation results for thermal PEB bias. In a 193 nm CAR in Fig. 20 (a) and a 248 nm CAR in Fig. 20 (b), PEB effects for C/ H pattern of 1:1 line and space are different

with those of other patterns. In both of CARs, PEB time is more controllable than PEB temperature for CD shrinkage. Thermal PEB biases depended on pattern types is same as thermal SB biases, so that

$$f_{PEB}^2(R) = \begin{cases} 1 & \textit{for isolated pattern} , \\ \alpha_2 & \textit{for dense patterns} \end{cases} \tag{64}$$

where α_2 is constant. When PEB temperature is at a target temperature, the function of PEB biases depended on PEB time is an exponential function of PEB time, so the thermal bias of PEB can be represented as:

$$f_{SB(or\ PEB)}^2(t) = [\alpha_3 \bullet \exp(\alpha_4 t)], \tag{65}$$

where α_3 and α_4 are constant values. Hence, For SB and PEB, thermal biases ($\Delta CD_{SB(or\ PEB)}$) of Eq. (60) based an orthogonal function can be represented as

$$(\Delta CD)_{SB}^2 = f_{SB}^2(R), \tag{66}$$

$$(\Delta CD)_{PEB}^2 = f_{PEB}^2(R) \bullet f_{PEB}^2(t), \tag{67}$$
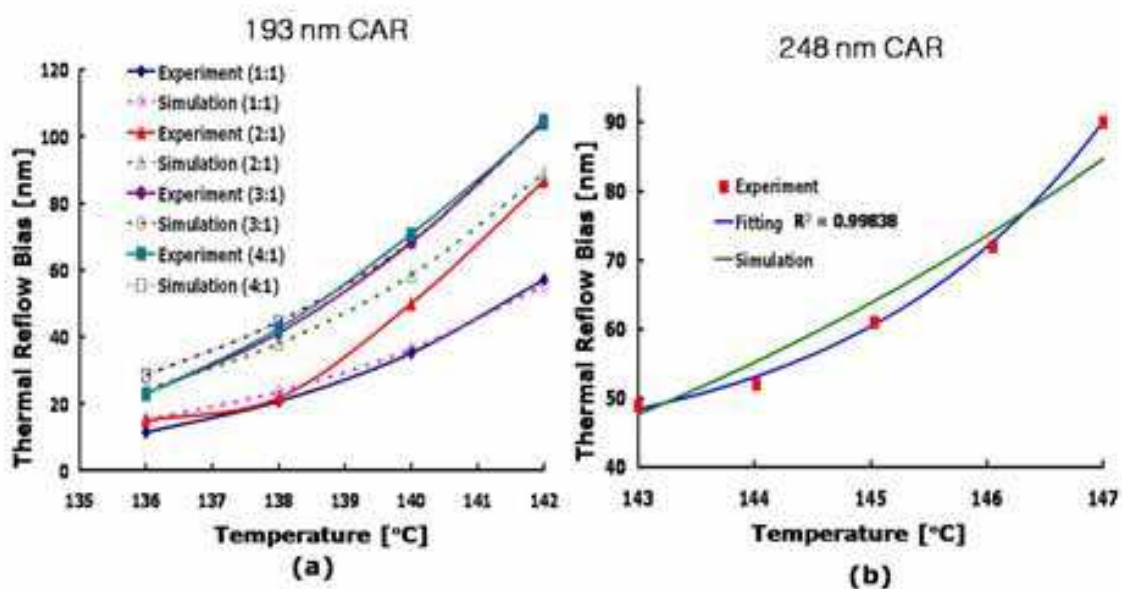

Fig. 21. Comparison between experiment results and simulation results for thermal reflow biases depended on temperature and pitch sizes in a ArF 193 nm CAR and a KrF 248 nm CAR.

Figure 21 shows the comparison between experiment results and simulation results of thermal reflow biases depended on temperature and pitch sizes in a 193 nm CAR in Fig. 21 (a) and a 248 nm CAR in Fig. 21 (b). Simulated results agree well with the experimental results in a small error range. The simulated function of thermal bias for a 193 nm CAR is

$$\begin{aligned}(\Delta CD)_{Thermal\ reflow}^2 &= [\alpha_1 \bullet \exp(\alpha_2/T)][\alpha_3 \bullet \exp(\alpha_4 R)] \\ &= [3.696 \times 10^{29} \bullet \exp(-8347.64393/T)][1.88152 \bullet \exp(-1.90217 \bullet R)]\end{aligned} \tag{68}$$

The simulated function of thermal bias depended on temperature for a 248 nm CAR is

$$(\Delta CD)^2_{Thermal\ reflow}(T) = \left[\alpha_1 \bullet \exp(\alpha_2 / T)\right] = \left[6.9796 \times 10^{25} \bullet \exp(-7429.2622 / T)\right]. \quad (69)$$
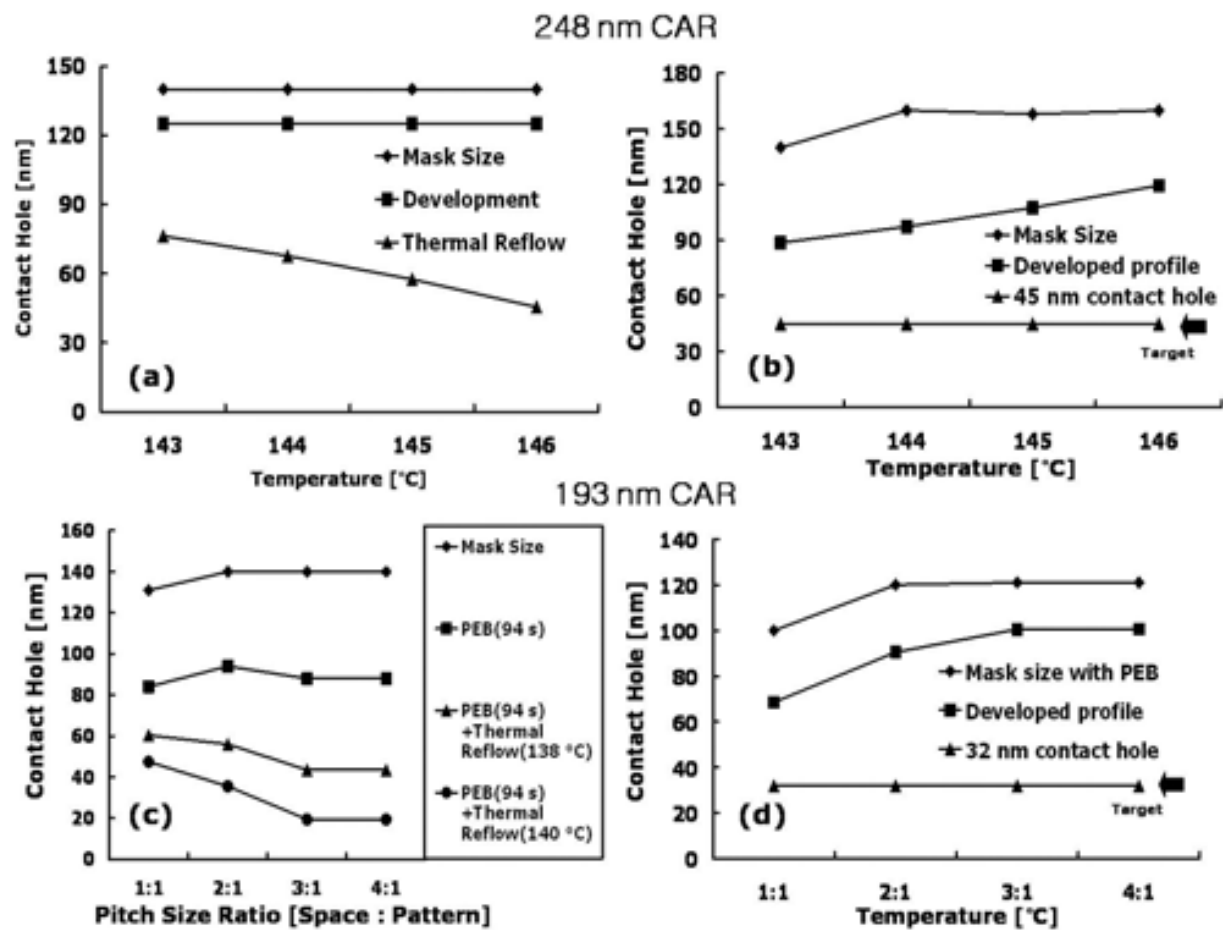

Fig. 22. Simulation results by using the orthogonal function method as an OPC method for a KrF 248 nm CAR in Figs. 22 (a) and (b) and a ArF 193 nm CAR in Figs. 22 (c) and (d).

Figure 22 shows simulation results by using the orthogonal function method as an OPC method. For a 248 nm CAR, 140 nm mask pattern size is shrunk down between 76.2 nm and 45.5 nm depended on the temperature of thermal reflow in Fig. 22 (a). When target pattern size is 45 nm in Fig. 22 (b), mask pattern size can be between 140 nm and 160 nm due to the temperature of thermal reflow. For a 193 nm CAR, mask pattern sizes between 131 nm and 140 nm can be shrunk down between 60.41 mm and 88 nm depended on pitch size ratio by using 138 °C temperature of thermal reflow in Fig. 22 (c). Also, those mask patterns can be reduced down between 47.46 nm and 19.42 nm depended on pitch size ratio by using 140 °C temperature of thermal reflow. When target pattern size is 32 nm in Fig. 22 (d), mask pattern size can be between 100 nm and 121 nm due to pitch size ratio.

5. Conclusion

Thermal treatment is a new process-extension technique using current-day lithography equipment and a chemically amplified resist. Thermal processes, such as softbake, post-

exposure bake, and thermal reflow process, are modelled from the chemical and physical behaviors of the CAR. For each thickness reduction, the simulated results agree well with the experimental results. For small pattern formation, the thermal effects move the boundaries of the resist bulk images to a horizontal point and make the boundaries dense. For line and space patterns, an underbake of SB and an overbake of PEB can be used for 45-nm pattern formation. For contact hole patterns, an underbake of PEB and thermal reflow can reduce the critical dimension. Although the CD sensitivity of the thermal parameters can be different due to other process parameters, thermal reflow is more effective method than the other two thermal processes. However, the optical proximity effect is quite severe when thermal processes are used for 45-nm patterns, so a model-based optical proximity correction is required for each thermal processes.

Hence, the orthogonal functions of thermal biases depended on temperature (or time) and pitch size are assumed and defined by using experimental data. Simulated results of thermal reflow for contact hole agree well with the experimental results in a small error range according to the baking temperature, time, and pitch size. For C/ H patterns, underbake PEB and thermal reflow can be formed 32 nm pattern for a ArF 193 nm CAR and 45 nm pattern for a KrF 248 nm CAR. An orthogonal functional method is useful to deal with OPC of thermal effects.

6. References

[1] Sigma-C: http://www.solid-c.de.

[2] C. A. Mack, "Inside PROLITH: A Compreshensive Guide to Optical Lithography Simulation", FINLE Technologies (Austin, TX: 1997).

[3] S. I. Lee, K.C. Ng, T. Orimoto, J. Pittenger, T. Horie, K. Adam, M. Cheng, E. Croffie, Y. Deng, F. Gennari, T. Pistor, G. Robins, M. Williamson, B. Wu, L. Yuan and R. Neureuther, "LAVA web-based remote simulation: enhancements for education and technology innovation," Proc. SPIE 4346, 1500 (2001): http://cuervo.eecs.berkeley.edu/Volcano.

[4] KLA-Tencor, FINLE Division, "Introduction to the PROLITH Toolkit,": http://www.kla-tencor.com.

[5] J. D. Byers, M. D. Smith, C. A. Mack, and J. J. Biafore, "Modeling soft-bake effects in chemically amplified resists", SPIE 5039, 1143 (2003).

[6] G. Thallikar, H. Liao, T. S. Cale, and F. R. Myers, "Experimental and simulation studies of thermal flow of borophosphosilicate and phosphosilicate glasses," J. Vac. Sci. Technol. B 13, 1875 (1995).

[7] D. Kang, S. Robertson and E. Pavelchek, "Simulation of 193 nm photoresists based on different polymer platforms," SPIE 4345, 936 (2001).

[8] D. Kang, S. Robertson, M. Reilly and E. Pavelchek, "Effects of mask bias on the mask error enhancement factor (MEEF) of contact holes," SPIE 4346, 858 (2001).

[9] H.-R Kim, Y.-B. Ahn, J. Kim, S. Kim, D. Park and Y.-S. Kim, "Implementation of contact hole patterning performance with KrF resist flow process for 60nm node DRAM application," Proc. SPIE 6154, 615441 (2006).

[10] C-W. Koh, D-H. Lee, M-S. Kim, S-N. Park, and W-K. Kwon, "Characterization of resist flow process for the improvement of contact hole CD uniformity," SPIE 5039, 1382 (2003).

[11] J-S. Kim, J-C. Jung, K-K. Kong, G. Lee, S-K. Lee, Y-S. Hwang, and K-S. Shin, "Contact hole patterning performance of ArF Resist for 0.l0 μm technology node," Proc. SPIE 4690, 577 (2002).
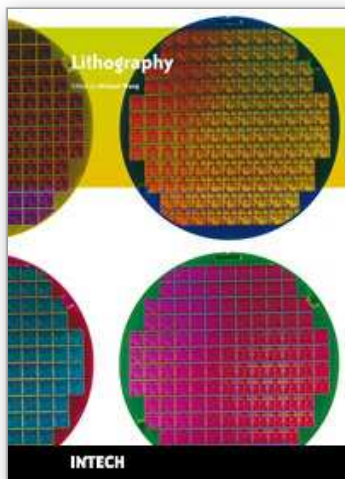
Lithography

Edited by Michael Wang

ISBN 978-953-307-064-3

Hard cover, 656 pages

Publisher InTech

Published online 01, February, 2010

Published in print edition February, 2010

Lithography, the fundamental fabrication process of semiconductor devices, plays a critical role in micro- and nano-fabrications and the revolution in high density integrated circuits. This book is the result of inspirations and contributions from many researchers worldwide. Although the inclusion of the book chapters may not be a complete representation of all lithographic arts, it does represent a good collection of contributions in this field. We hope readers will enjoy reading the book as much as we have enjoyed bringing it together. We would like to thank all contributors and authors of this book.

How to reference

In order to correctly reference this scholarly work, feel free to copy and paste the following:

Sang-Kon Kim (2010). A Method for Optical Proximity Correction of Thermal Processes: Orthogonal Functional Method, Lithography, Michael Wang (Ed.), ISBN: 978-953-307-064-3, InTech, Available from: http://www.intechopen.com/books/lithography/a-method-for-optical-proximity-correction-of-thermal-processes-orthogonal-functional-method